

A mathematical model of endothelial progenitor cell cluster formation during the early stages of vasculogenesis

Chiara Villa* Alf Gerisch† Mark A. J. Chaplain‡

Abstract

The formation of new vascular networks is essential for tissue development and regeneration, in addition to playing a key role in pathological settings such as ischemia and tumour development. Experimental findings in the past two decades have led to the identification of a new mechanism of neovascularisation, known as cluster-based vasculogenesis, during which endothelial progenitor cells (EPCs) mobilised from the bone marrow are capable of bridging distant vascular beds in a variety of hypoxic settings *in vivo*. This process is characterised by the formation of EPC clusters during its early stages and, while much progress has been made in identifying various mechanisms underlying cluster formation, we are still far from a comprehensive description of such spatio-temporal dynamics. In order to achieve this, we propose a mathematical model of the early stages of cluster-based vasculogenesis, comprising of a system of non-local partial differential equations including key mechanisms such as endogenous chemotaxis, matrix degradation, cell proliferation and cell-to-cell adhesion. We conduct a linear stability analysis on the system, solve the equations numerically and conduct a sensitivity analysis to investigate the role of underlying dynamics on the speed of cluster formation and the size of clusters, measured via appropriate metrics. Our results, which qualitatively compare with data from *in vitro* experiments, elucidate the complementary role played by endogenous chemotaxis and matrix degradation in the formation and topology of clusters, indicating promising, fruitful future modelling and experimental research perspectives.

1 Introduction

The formation of new vascular networks is essential for tissue development and regeneration, as a functional vasculature is critical for tissue homeostasis. It is responsible for the delivery of oxygen and nutrients as well as the disposal of waste products. In addition, neovascularisation of local tissue is critical in a variety of pathological processes, among which are retinopathy, tumour growth, wound healing and soft-tissue ischemia. The development of a vascular network in localised solid tumours is particularly well known to promote further tumour growth and metastases. Therefore a better understanding of the mechanisms governing neovascularisation can help improve current therapeutic strategies, as well as identify new ones.

The two fundamental processes of neovascularisation are known as *vasculogenesis*, the *de novo* formation of a new vascular network, and *angiogenesis*, the formation of new blood vessels from pre-existing ones. While the distinction between these two processes has been clear since the early days of the field of study of vascular development [51], for a long time the term vasculogenesis was only associated with endothelial progenitor cells (EPCs)-mediated embryonic vasculogenesis, while blood vessels formation in adult organisms was believed to be formed predominantly, if not exclusively, via angiogenesis [48]. In the past 20 years great progress was made in understanding neovascularisation processes, in particular with the discovery of bone marrow-derived

*School of Mathematics and Statistics, University of St Andrews, UK (cv23@st-andrews.ac.uk)

†Department of Mathematics, Technische Universität Darmstadt, Germany (gerisch@mathematik.tu-darmstadt.de)

‡School of Mathematics and Statistics, University of St Andrews, UK (majc@st-andrews.ac.uk)

EPCs and postnatal vasculogenesis [8, 10, 9, 32, 46, 48, 58], for which a specific mechanism, here referred to as *cluster-based vasculogenesis*, has recently been proposed. This newly identified mechanism of neovascularisation has been observed only in hypoxic settings *in vivo*, from development [47] to soft-tissue ischemia [63] to tumour vascularisation [68], and has been studied in detail by Blatchley *et al.* [12] in hypoxic gradients *in vitro*.

1.1 Cluster-based vasculogenesis

During this process, after recruitment of EPCs residing in the bone marrow to the hypoxic site [9, 58], EPCs first organise into clusters and then form the new vascular network by sprouting from these clusters and merging with the pre-existing vasculature, often in combination with angiogenesis. The term “cluster-based” vasculogenesis was therefore proposed by Blatchley and coworkers [12] to highlight the key step of the process which well distinguishes it from classical “single-cell” vasculogenesis, during which sparse mature endothelial cells (ECs) directly reorganise into a vascular network [56].

While EPCs recruitment to angiogenic sites has been well studied, we are still far from understanding how clusters form and what drives sprouting from these clusters. Akita *et al.* [1] reported that EPC differentiation, secretion of angiogenic factors – such as Vascular Endothelial Growth Factor (VEGF) – and migration were enhanced by hypoxic conditioning, resulting in increased EPC cluster formation in hypoxia *in vitro*. Nevertheless, it was not until recently that Blatchley and coworkers proposed, together with the name here used, a two-step mechanism of cluster formation and stabilisation in hypoxic environments [12]. This relies on the observation that in highly hypoxic environments the production of matrix metalloproteases (MMPs) is upregulated by the presence of reactive oxygen species (ROS), resulting in significant extracellular matrix (ECM) degradation responsible for EPCs aggregation into clusters, which are then stabilised by cell-to-cell adhesion. EPC clusters were observed between 24 and 48 hours from the beginning of the experiments, presenting diameters in the range 100–400 μm . Finally, after 48 hours, cell-to-matrix interactions lead to sprouting and network formation, particularly fostered by highly viscoelastic – where not degraded – ECM. The final network, observed after 72 hours, was reported to be up to 500 μm in length, larger than previously observed ones formed via angiogenesis or single-cell vasculogenesis. Overall, cluster-based vasculogenesis has been shown to be of great importance in highly hypoxic tissues, as EPC clusters form in these regions far from pre-existing blood vessels and, after sprouting, function as a bridge for distant vascular beds, allowing for neovascularisation in physiological and pathological settings in which angiogenesis alone would not have sufficed.

While this is a great step forward in the understanding of cluster-based vasculogenesis, much further work is required to reach an exhaustive comprehension of the process, as well as to unlock its full potential in therapeutic interventions in a variety of pathological process. On this regard, mathematical modelling can help elucidate the mechanisms behind network formation, serving as a proof of concept mean for newly developed theories [57], as well as steer experimental investigations towards the most promising research perspectives.

1.2 Mathematical modelling of vasculogenesis

While the mathematical model presented here is the first one formulated to study cluster-based vasculogenesis, many have been proposed to investigate single-cell vasculogenesis observed by Serini *et al.* [56] – see [3, 53] for detailed reviews. In particular, continuum deterministic models in the extant literature can be categorised as either modelling the early stages of single-cell vasculogenesis, characterised by persistence of motion and endogenous chemotaxis and thus referred to as PEC models [4, 17, 22, 33, 56], or the late stages of this process, during which the mechanical interaction between the cells and the ECM cannot be neglected, thus comprising of mechanochemical models [37, 40, 41, 42], with the exception of the work by Tosin *et al.* [65] who proposed a comprehensive model.

PEC models include an explicit description of VEGF dynamics, friction between cells and substrate, pressure generated by tightly packed cells, and omit cell proliferation and death since they refer to *in vitro* dynamics

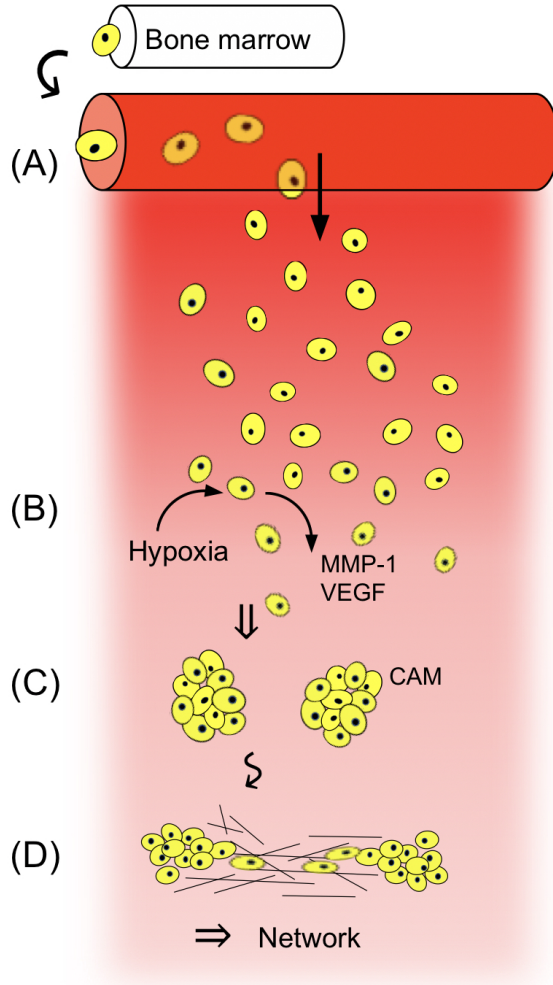


Figure 1: Summary of the steps of cluster-based vasculogenesis: (A) EPCs in the bone-marrow enter the circulation and reach the hypoxic site; (B) local hypoxia fosters EPC production of matrix degrading enzymes (MMP-1) and chemotactic agents (VEGF); (C) clusters form and are stabilised by cell-adhesion molecules (CAM); (D) cell-matrix interactions increase, sprouting from clusters occurs and a vascular network forms.

of mature ECs on a relatively short timescale. Such models have so far helped to extrapolate information underlying the origin and structure of newly formed vascular networks, for instance relating the characteristic chord length ℓ to the VEGF diffusion coefficient D_c and decay rate λ_c with the formula $\ell = \sqrt{D_c(\lambda_c)^{-1}}$ [4, 3, 22, 56], or investigating the minimum – and maximum – initial cell density required for network assembly and the observation of a phenomenon known as percolative transition [3, 17, 22, 33, 56]. On the other hand, mechanochemical models of vasculogenesis highlighted the role of cell traction and ECM stiffness, as well as the initial cell density, in the formation of lacunae or – in case of very low stiffness or very high traction – clusters. These models in fact not only include chemotaxis and diffusion, but also haptotaxis, advection, strain dependent movement, cell traction on the ECM – generally modelled as a linear viscoelastic material – and external viscous drag or elastic forces [3, 37, 40, 41, 42, 53, 65].

We here extend mathematical models of vascular network assembly to investigate the early stages of cluster-based vasculogenesis, during which mechanical interactions between EPCs and the ECM can be neglected. We present a continuum deterministic model of EPC cluster formation, comprising of a system of partial differential equation modelling dynamics such as endogenous chemotaxis, MMP-mediated ECM degradation, nonlocal cell-to-cell and cell-to-matrix adhesion, EPC diffusion, proliferation and death, together with annexed ECM, VEGF and MMP dynamics. Our model provides a theoretical basis for a comprehensive description of the mechanisms underlying cluster formation, clarifying the role played by different dynamics and elucidating the determinants of cluster size with the introduction of appropriate metrics.

In Section 2 we describe the mathematical model in detail, together with the analytical method used to investigate the system and the numerical method used to obtain solutions, and introduce the metrics defined to study cluster size. In Section 3 we report the analytical results, followed by detailed numerical investigations of the cluster formation process and the size of clusters in 1D and 2D, which are qualitatively compared with the experimental findings of Blatchley *et al.* [12]. In Section 4 we summarise the main findings and discuss future research perspectives.

2 Methods

2.1 Mathematical model

Let $t \in \mathbb{R}_{\geq 0}$ indicate time and $\mathbf{x} \in \mathbb{R}^2$ position in space. We will consider the dynamics in a two-dimensional (2D) spatial domain $\Omega \subset \mathbb{R}^2$, as well as the corresponding one-dimensional (1D) problem, for which we make use of the notation $x \in \mathbb{R}$ to indicate space. Unless indicated otherwise, all definitions introduced in this section for the 2D problem hold for the corresponding 1D one. The density of EPCs at time t and position \mathbf{x} is given by $n(t, \mathbf{x})$, in units of cell cm^{-3} , and the ECM density by $\rho(t, \mathbf{x})$, in units of nM. Similarly we indicate the concentration of a matrix-degrading enzyme, such as MMP-1, by $m(t, \mathbf{x})$, in units of $\mu\text{g cm}^{-3}$, and that of a chemotactic agent, such as VEGF-A, by $c(t, \mathbf{x})$, in units of ng cm^{-3} . We also introduce the vector of independent variables $\mathbf{v}(t, \mathbf{x}) := (n(t, \mathbf{x}), \rho(t, \mathbf{x}), m(t, \mathbf{x}), c(t, \mathbf{x}))^\top$. Our model then consists of a system of mass-balance equations, one for each independent variable introduced.

2.1.1 EPC density dynamics

The mass-balance equation for the density of EPCs is of the form:

$$\partial_t n + \nabla \cdot [\mathbf{J}_d(n) + \mathbf{J}_c(n, c) + \mathbf{J}_a(\mathbf{v})] = pn(1 - \vartheta_1 n - \vartheta_2 \rho), \quad (1)$$

where $\mathbf{J}_d(n)$ models spatial diffusion to account for random movement of cells, $\mathbf{J}_c(n, c)$ indicates the chemotactic flux in response to VEGF gradients and $\mathbf{J}_a(\mathbf{v})$ the advective flux due to cell-to-cell and cell-to-matrix adhesion, while the term on the right-hand side of the equation models cell proliferation and death. In particular, we consider a modified version of the standard logistic growth, as proposed by Gerisch and Chaplain [25], in which EPCs proliferate at rate $p \in \mathbb{R}_{\geq 0}$ and die due to competition for space – occupied by both cells and ECM – and resources. Parameters $\vartheta_1 \in \mathbb{R}_{> 0}$ and $\vartheta_2 \in \mathbb{R}_{> 0}$ indicate the fraction of one unit volume of physical space occupied by EPCs at unit density and by ECM at unit density respectively, such that $(\vartheta_1 n + \vartheta_2 \rho)$ indicates the total fraction of locally occupied space.

Spatial diffusion and chemotaxis A number of variations of the classic Patlak–Keller–Segel model of diffusion and chemotaxis [29, 43], which is well-known for having solutions that blow up in finite time, have

been proposed in the literature [14, 43]. We hereby consider a modified version of the forms proposed by Hillen and Painter [27, 44], making use of the following definitions:

$$\mathbf{J}_d(n) = -D_n \nabla n, \quad \mathbf{J}_c(n, c) = \chi n (1 - \vartheta_1 n - \vartheta_2 \rho)_+ \nabla c, \quad (2)$$

where we have used $(\cdot)_+ := \max(0, \cdot)$. In definitions (2) spatial diffusion follows Fick's law, with diffusivity $D_n \in \mathbb{R}_{\geq 0}$, while chemotaxis is modelled as an advective flux of cells up the gradient of the chemotactic agent concentration c , modulated by the chemotactic sensitivity of cells. This is proportional to the chemotactic sensitivity coefficient $\chi \in \mathbb{R}_{\geq 0}$ and the locally available space, given by $(1 - \vartheta_1 n - \vartheta_2 \rho)_+$, in order to account for overcrowding effects which impede the cells to move in response to chemotactic gradients, to the extent that if the space is locally full no chemotaxis can occur.

Cell-to-cell and cell-to-matrix adhesion We model cell-to-cell and cell-to-matrix adhesion in the continuous form proposed by Armstrong *et al.* [7] for one and multiple cell populations, and adapted by Gerisch and Chaplain [25] to account for adhesion to the ECM in the context of tumour invasion. The advective flux due to cell-to-cell and cell-to-matrix adhesion in (1) is therefore given by

$$\mathbf{J}_a(\mathbf{v}) = n \mathcal{A}[\mathbf{v}(t, \cdot)] \quad (3)$$

where $\mathcal{A}[\mathbf{v}(t, \cdot)]$ is the adhesion velocity at some point \mathbf{x} , which is an operator acting on $\mathbf{v}(t, \cdot)$ defined as a function of \mathbf{x} . For problems in 1D this is defined as

$$\mathcal{A}[\mathbf{v}(t, \cdot)](x) := \frac{1}{R} \int_0^R \sum_{j=0}^1 \eta(j) \Gamma(r) g(\mathbf{v}(t, x + r\eta(j))) dr, \quad (4)$$

while for problems in 2D it is defined as

$$\mathcal{A}[\mathbf{v}(t, \cdot)](\mathbf{x}) := \frac{1}{R} \int_0^R r \int_0^{2\pi} \boldsymbol{\eta}(\theta) \Gamma(r) g(\mathbf{v}(t, \mathbf{x} + r\boldsymbol{\eta}(\theta))) d\theta dr. \quad (5)$$

In equation (4) $\eta(j) = (-1)^j$ with $j = 0, 1$ indicates the 1D right and left unit outer normal vector, while in equation (5) the 2D unit outer normal vector corresponding to angle θ is given by $\boldsymbol{\eta}(\theta) = (\cos \theta, \sin \theta)^\top$. In definitions (4) and (5), we have that the sensing region of cells at position $\mathbf{x} \in \mathbb{R}^d$ ($d = 1, 2$) is the d -dimensional ball centred in \mathbf{x} with radius $R > 0$, called the sensing radius. Then $\Gamma(r)$ is the radial dependency function, indicating how strong the adhesion velocity at a point \mathbf{x} is influenced by points at a distance $r \leq R$ from the centre \mathbf{x} of the sensing region. Assuming $\Gamma(r)$ decays linearly with r to be zero at the boundary of the sensing region, we here make use of the forms proposed by Gerisch and Chaplain [25]

$$\Gamma(r) = \frac{1}{R} \left(1 - \frac{r}{R}\right) \quad \text{and} \quad \Gamma(r) = \frac{3}{\pi R^2} \left(1 - \frac{r}{R}\right) \quad (6)$$

in the 1D and 2D problems respectively. Finally, in both (4) and (5) the non-local term $g(\mathbf{v})$ represents the velocity of the cells at \mathbf{x} due to adhesions to other cells or the ECM in the sensing region of \mathbf{x} . This is given by

$$g(\mathbf{v}) := g(n, \rho) = (S_{nn}n + S_{n\rho}\rho) (1 - \vartheta_1 n - \vartheta_2 \rho)_+, \quad (7)$$

in which $S_{nn} \in \mathbb{R}_{\geq 0}$ and $S_{n\rho} \in \mathbb{R}_{\geq 0}$ are the cell-to-cell and cell-to-matrix adhesion coefficients respectively, while ϑ_1 and ϑ_2 are the same as in (1) and (2). The first term in definition (7) indicates that at each point in the sensing region the higher the density of EPCs or ECM is, the higher the number of adhesion sites present will be, and the higher the contribution to the adhesion velocity will be. On the other hand, the last term in equation (7) ensures that the adhesion velocity is modulated by overcrowding effects, since a point in space

too densely packed by EPCs or ECM could imply that many adhesion sites are unavailable or that the cells at position \mathbf{x} may struggle to sense the available ones and move in that direction.

2.1.2 ECM density dynamics

We let the matrix be degraded by matrix-degrading enzymes at a rate $\gamma \in \mathbb{R}_{\geq 0}$ and account for ECM remodelling at a rate $\mu \in \mathbb{R}_{\geq 0}$, resulting in the following mass-balance equation for the ECM density:

$$\partial_t \rho = -\gamma \rho m + \mu(1 - \vartheta_1 n - \vartheta_2 \rho)_+, \quad (8)$$

where the parameters ϑ_1 and ϑ_2 have already been introduced in Section 2.1.2, indicating ECM remodelling is here understood as a restructuring phenomenon that only occurs if space is available [21].

2.1.3 MMP concentration dynamics

We let the matrix-degrading enzyme (MMP) be produced by the EPCs at a rate $\alpha_m \in \mathbb{R}_{\geq 0}$, undergo Fickian diffusion with diffusivity $D_m \in \mathbb{R}_{\geq 0}$, and decay at rate $\lambda_m \in \mathbb{R}_{\geq 0}$. Then the MMP concentration $m(t, \mathbf{x})$ satisfies:

$$\partial_t m - D_m \Delta m = \alpha_m n - \lambda_m m. \quad (9)$$

Note that, in view of the experimental evidence presented in [12], the MMP production rate α_m is correlated with the local level of hypoxia.

2.1.4 VEGF concentration dynamics

Similarly to the matrix-degrading enzyme, we let the chemotactic agent (VEGF) be produced by the EPCs at a rate $\alpha_c \in \mathbb{R}_{\geq 0}$, undergo Fickian diffusion with diffusivity $D_c \in \mathbb{R}_{\geq 0}$, and decay at rate $\lambda_c \in \mathbb{R}_{\geq 0}$. This results in the following mass-balance equation for the VEGF concentration $c(t, \mathbf{x})$:

$$\partial_t c - D_c \Delta c = \alpha_c n - \lambda_c c. \quad (10)$$

In view of the experimental evidence presented in [1], the VEGF production rate α_c is correlated with the local level of hypoxia.

2.1.5 Boundary conditions

While equation (8) describes the dynamics of the ECM in the closed spatial domain $\bar{\Omega} = \Omega \cup \partial\Omega$, equations (1), (9) and (10) are posed on the open set Ω , and are complemented with zero-flux boundary conditions.

2.1.6 Initial conditions

As proposed by Serini *et al.* [56], we construct the initial conditions to mimic sparsely distributed cells on the ECM. In particular, the initial cell density is given by the sum of $K \in \mathbb{N}$ randomly distributed bell-shaped bumps. In particular, we construct these bumps as Gaussian-like functions with maximum height and full width at half maximum (FWHM) both equal to the size of an average cell diameter $a \in \mathbb{R}_{> 0}$. We let the initial ECM density be constant and the initial MMP and VEGF concentrations be null. Thus we have

$$n(t, \mathbf{x}) = \sum_{i=1}^K G_i(\mathbf{x}; a), \quad \rho(0, \mathbf{x}) = \rho_0 > 0, \quad m(0, \mathbf{x}) = c(0, \mathbf{x}) = 0, \quad (11)$$

where $G_i(\mathbf{x}; a)$ indicates the Gaussian-like function centered at the (randomly selected) $\mathbf{x}^{(i)} \in \Omega$ and is given by

$$\begin{aligned} G_i(x; a) &:= a \exp \left[-\frac{4 \ln 2}{a^2} (x - x^{(i)})^2 \right] & \text{for } x \in \Omega \subset \mathbb{R}, \\ G_i(\mathbf{x}; a) &:= a \exp \left[-\frac{4 \ln 2}{a^2} |\mathbf{x} - \mathbf{x}^{(i)}|^2 \right] & \text{for } \mathbf{x} \in \Omega \subset \mathbb{R}^2, \end{aligned} \quad (12)$$

for the 1D and 2D problem respectively. In equation (12) we have used the formula $\text{FWHM} = 2\sqrt{2 \ln 2} \sigma$ where σ is the standard deviation of the Gaussian.

2.2 Nondimensional model and baseline parameter set

We nondimensionalise the system of equations (1) and (8)-(10), together with definitions (2)-(7), (11) and (12), by letting

$$\hat{t} = \frac{t}{\tau}, \quad \hat{\mathbf{x}} = \frac{\mathbf{x}}{L}, \quad \hat{n} = \frac{n}{N}, \quad \hat{\rho} = \frac{\rho}{P}, \quad \hat{m} = \frac{m}{M}, \quad \hat{c} = \frac{c}{C}.$$

We use $L = 0.1$ cm as characteristic length scale, in accordance with previous vasculogenesis works [56, 37] and for easy visual comparison with the experimental results reported by Blatchley and coworkers [12]. We then take reference time scale $\tau := L^2/D$, where D is a characteristic diffusion coefficient $D \sim 10^{-6}$ cm²s⁻¹ [13], resulting in a reference time scale $\tau = 10^4$ s. The reference cell density is chosen to be $N := n_M = \vartheta_1^{-1}$ and we take $\vartheta_1 = 10^{-9}$ cm³/cell, the average volume occupied by an endothelial cell [49]. We use a reference matrix density of $P = 10^{-1}$ nM [6, 5, 64] and define the parameter $\vartheta_2 := P^{-1}$. We take the reference VEGF density to be $C = 20$ ng cm⁻³, in the range of values generally considered in *in vitro* set ups [26, 35, 56]. Finally, Blatchley *et al.* [12] reported concentrations of MMP-1 in the range $1 - 100$ $\mu\text{g ml}^{-1}$, so we take the intermediate concentration as reference MMP density, *i.e.* $M = 10$ $\mu\text{g cm}^{-3}$. Let us introduce the following nondimensional parameters:

$$\begin{aligned} \hat{D}_n &= \frac{D_n}{D}, \quad \hat{\chi} = \frac{\chi C}{D}, \quad \hat{R} = \frac{R}{L}, \quad \hat{S}_{nn} = \frac{S_{nn}}{D\vartheta_1}, \quad \hat{S}_{n\rho} = \frac{S_{n\rho}}{D\vartheta_2}, \quad \hat{p} = p\tau, \quad \hat{\gamma} = \gamma M\tau, \quad \hat{\mu} = \mu\tau\vartheta_2, \\ \hat{D}_m &= \frac{D_m}{D}, \quad \hat{\alpha}_m = \frac{\alpha_m\tau}{M\vartheta_1}, \quad \hat{\lambda}_m = \lambda_m\tau, \quad \hat{D}_c = \frac{D_c}{D}, \quad \hat{\alpha}_c = \frac{\alpha_c\tau}{C\vartheta_1}, \quad \hat{\lambda}_c = \lambda_c\tau, \quad \hat{a} = \frac{a}{L}, \quad \hat{\rho}_0 = \frac{\rho_0}{P}. \end{aligned}$$

Then the overall nondimensionalised system becomes, dropping hats for convenience,

$$\left\{ \begin{array}{l} \partial_t n = D_n \Delta n - \chi \nabla \cdot (n(1-n-\rho)_+ \nabla c) - \nabla \cdot (n \mathcal{A}[\mathbf{v}(t, \cdot)]) + pn(1-n-\rho) \\ \partial_t \rho = -\gamma \rho m + \mu(1-n-\rho)_+ \\ \partial_t m = D_m \Delta m + \alpha_m n - \lambda_m m \\ \partial_t c = D_c \Delta c + \alpha_c n - \lambda_c c \end{array} \right. \quad (13)$$

where (13)₁, (13)₃ and (13)₄ are posed on $(t, \mathbf{x}) \in (0, \infty) \times \Omega$ and are complemented by zero Neumann BCs on $\partial\Omega$, while (13)₂ is posed on $(t, \mathbf{x}) \in (0, \infty) \times \bar{\Omega}$. In equation (13) the operator $\mathcal{A}[\mathbf{v}(t, \cdot)]$ takes the form (4) in 1D and (5) in 2D, with $\Gamma(r)$ still defined as in (6), and $g(\mathbf{v})$ in (7) now given by

$$g(\mathbf{v}) = g(n, \rho) = (S_{nn}n + S_{n\rho}\rho) (1 - n - \rho)_+, \quad (14)$$

in which the parameters R , S_{nn} and $S_{n\rho}$ are the nondimensional ones introduced above, and the system (13) is complemented with initial conditions (11)-(12), in which the parameters a and ρ_0 now corresponds to the nondimensional ones introduced above. The baseline parameter set, with the corresponding nondimensional (ND) parameter values, is reported in Table 1 – see A for details.

Table 1: Baseline parameter set (ND = Nondimensional value)

Parameter	Dimensional value	ND	Description	Ref.
ϑ_1	10^{-9} cm ³ /cell		Average cell volume	[49]
ϑ_2^{-1}	10^{-1} nM		Reference ECM density	[6, 5, 64]
D	10^{-6} cm ² s ⁻¹		Reference diffusion rate	[13]
D_n	10^{-9} cm ² s ⁻¹	10^{-3}	EPC diffusion coefficient	[3]
χ	1.4×10^{-7} cm ⁵ ng ⁻¹ s ⁻¹	2.8	Chemotactic coefficient	[28]
R	5×10^{-3} cm	0.05	Cell sensing radius	[55]
S_{nn}	10^{-16} cm ⁵ s ⁻¹	0.1	Cell-to-cell adhesion coefficient	[25]
$S_{n\rho}$	10^{-6} cm ² nM ⁻¹ s ⁻¹	0.1	Cell-to-matrix adhesion coefficient	[25]
p	10^{-5} s ⁻¹	1	Cell proliferation rate	[31]
γ	9×10^5 cm ³ g ⁻¹ s ⁻¹	0.2	ECM degradation rate	[30]
μ	0.2×10^{-5} nM s ⁻¹	0.2	Rate of ECM remodelling	[19, 21, 25]
D_m	8×10^{-9} cm ² s ⁻¹	8×10^{-3}	MMP diffusion coefficient	[52]
α_m	0.5×10^{-12} μ g s ⁻¹	0.5	MMP production rate	[6, 19, 21, 25]
λ_m	5×10^{-5} s ⁻¹	0.5	MMP decay rate	[30]
D_c	10^{-7} cm ² s ⁻¹	0.1	VEGF diffusion coefficient	[3, 22, 39, 56]
α_c	5×10^{-12} ng s ⁻¹	2.5	VEGF production rate	[70]
λ_c	$\lambda_c = 2.7 \times 10^{-4}$ s ⁻¹	2.7	VEGF decay rate	[56, 60]
a	10^{-3} cm	10^{-2}	Average cell diameter ($\sqrt[3]{\vartheta_1}$)	[49]
ρ_0	0.5×10^{-1} nM	0.5	Initial ECM density	Section 3.1

2.3 Linear stability analysis

We perform a linear stability analysis (LSA) on the spatially homogeneous steady states, say, $\bar{\mathbf{v}}$ of the nondimensional model (13)-(14), to gain insights into possible mechanism responsible for aggregation dynamics. During the LSA we first introduce a small spatially homogeneous perturbation $\mathbf{v} = \bar{\mathbf{v}} + \tilde{\mathbf{v}}(t)$, with $|\tilde{\mathbf{v}}| \ll 1$, in (13) and linearise. By assuming the small perturbation is proportional to $\exp(\sigma t)$, we derive a dispersion relation for σ and impose $\text{Re}(\sigma) < 0$, to ensure spatially homogeneous steady states are stable to spatially homogeneous perturbations. We then repeat these steps under a spatially inhomogeneous perturbation $\mathbf{v} = \bar{\mathbf{v}} + \tilde{\mathbf{v}}(t, \mathbf{x})$, with $|\tilde{\mathbf{v}}| \ll 1$, assuming it is proportional to $\exp(\sigma t + i\mathbf{k}x)$ – or $\tilde{\mathbf{v}}(t, \mathbf{x}) \propto \exp(\sigma t + i\mathbf{k} \cdot \mathbf{x})$ in 2D. Once we obtain a dispersion relation $\sigma(k^2)$ – where $k^2 = |\mathbf{k}|^2$ in 2D – we study the conditions under which $\text{Re}(\sigma(k^2)) > 0$ for some k^2 , as in such regimes we expect spatially inhomogeneous perturbations to grow in time and patterns to arise. We conduct this analysis both in 1D and 2D for the model (13)-(14), as well as for the corresponding problem in absence of saturation effects, *i.e.* substituting definition (2) for $\mathbf{J}_c(n, c)$ with

$$\mathbf{J}_c(n, c) := \chi n \nabla c, \quad (15)$$

and definition (14) for $g(\mathbf{v})$ with

$$g(\mathbf{v}) := g(n, \rho) = (S_{nn}n + S_{n\rho}\rho) . \quad (16)$$

2.4 Numerical method

We solve the nondimensional system (13)-(14) in $\Omega = (0, 1)$ in 1D and $\Omega = (0, 1) \times (0, 1)$ in 2D, with zero-flux boundary conditions and initial conditions (11)-(12). All numerical simulations have been performed in MATLAB. The numerical scheme follows the method of lines by first discretising the non-local model in space (with 1000 grid cells in 1D and 100×100 grid cells in 2D), yielding an initial value problem for a large system of ordinary differential equations. This system is then solved using the time integration scheme ROWMAP [69], implemented in a Fortran subroutine and called from MATLAB. For the discretisation in space we use a second-order finite volume approach which makes use of flux-limiting – here in particular we employ the Koren flux limiter ($k = 1/3$, $\delta = 0.25$) – for an accurate discretisation of the taxis and adhesion terms. We refer the interested reader to [24, 25] for more details of the numerical scheme – of the model short of the chemotactic dynamics – and of the treatment of the non-local terms, respectively.

2.5 Cluster size metrics

In order to gain insight into the role played by different biological, chemical and mechanical factors in dictating the clusters' size, we define two different measures of cluster size with complementary information, as similarly done in [45]. We define these for the nondimensional 1D problem, but analogous definitions can be considered for the 2D problem. Assume that $Q \in \mathbb{N}$ clusters have formed at time $t = T$ and let $\omega \subset \Omega$ be the subdomain supporting these clusters, *i.e.*

$$\omega := \text{supp } n(T, x) . \quad (17)$$

Then ω can be partitioned into Q subdomains $\omega_1, \dots, \omega_Q$, *i.e.* we have

$$\bigcup_{i=1}^Q \omega_i = \omega \quad \text{and} \quad \bigcap_{i=1}^Q \omega_i = \emptyset , \quad (18)$$

where each ω_i ($i = 1, \dots, Q$) corresponds to the support of a cluster. We let the average cluster *width* W and average cluster *compactness* C be defined by

$$W := \frac{1}{Q} \sum_{i=1}^Q W_i , \quad \text{where} \quad W_i := |\omega_i| \quad i = 1, \dots, Q , \quad (19)$$

$$C := \frac{1}{Q} \sum_{i=1}^Q C_i , \quad \text{where} \quad C_i = \frac{\int_{\omega_i} n(T, x) dx}{W_i} \quad i = 1, \dots, Q . \quad (20)$$

Under definitions (17)-(19), the width W_i ($i = 1, \dots, Q$) of each cluster is a measure of the length of its support, which may be understood as an indicator of the diameter of the cluster assuming the 1D case is reflective of the corresponding 2D problem. Note that the analogous 2D definition to (19) would inform us on the area covered by each cluster, from which the average cluster diameter could be calculated. However, this would need to be complemented with an additional metric for cluster elongation (*e.g.* the ratio between the diameter of the circle circumscribing ω_i and that of the one inscribed in ω_i), in order to obtain an exhaustive description of the cluster's topology. Under definition (20), in which $n(T, x)$ is the nondimensional cell density, the compactness C_i ($i = 1, \dots, Q$) of each cluster is a measure of the fraction of local volume occupied by cells, in the domain

dictated by the cluster’s support ω_i . Cluster compactness allows us to distinguish between simple cell aggregates and well-defined clusters, identified as such only if C is higher than 0.5, corresponding to at least half the local volume being occupied by cells. Under the choices of nondimensionalisation and of spatial domain for the numerical simulations, we expect $0 \leq W_i \leq 1$ and – under cell incompressibility assumptions – $0 \leq C_i \leq 1$ for all $i = 1, \dots, Q$. Figure 2 summarises the biological interpretation of possible combinations of W and C .

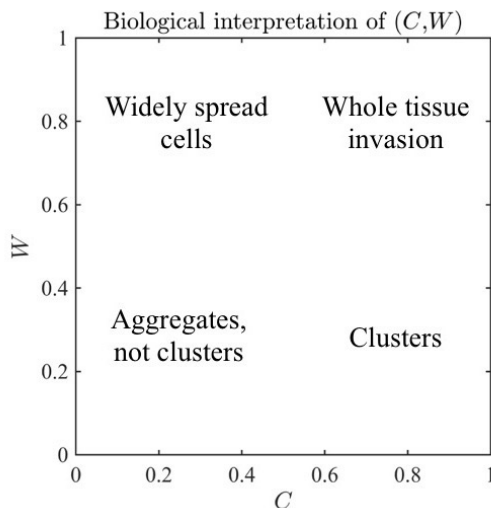


Figure 2: Biological interpretation of possible combinations of cluster width W (19) and cluster compactness C (20): high W and low C capture the scenario in which few cells are widely spread across the domain (top left region of the C - W plane); low W and low C capture the presence of loose cell aggregates, (bottom left region); low W and high C capture the presence of clusters (bottom right region); high W and high C capture the scenario in which many cells are widely spread across the domain, corresponding to the case of tissue invasion in which no clusters can be identified (top right region).

3 Results

We report in Section 3.1 the key results of the LSA, as described in Section 2.3, and in Sections 3.2-3.5 the results of the numerical simulations obtained using the method described in Section 2.4. In Section 3.2 we report the results of the 1D model under the baseline parameter set in Table 1 and qualitatively investigate the determinants of cluster formation in Section 3.3. In Section 3.4 we report the results of the sensitivity analysis conducted to elucidate the relation between different parameters and the average cluster width and compactness, as defined in Section 2.5. Finally, we report the results of the 2D model in Section 3.5.

3.1 Linear stability analysis results

We conducted a LSA on the system (13) under definitions (2) for chemotaxis and (4)-(7) for cell-to-cell and cell-to-matrix adhesion, as well as in the absence of saturation effects, that is under definitions (15) and (16) instead of (2) and (7), both in 1D and 2D. The full LSA can be found in the supplementary document ‘SuppInfo’ and the key results are summarised below.

The two spatially homogeneous steady states are such that either the whole domain is solely occupied by cells ($\bar{n} = 1$ and $\bar{\rho} = 0$) or solely occupied by matrix ($\bar{n} = 0$ and $\bar{\rho} = 1$). In absence of matrix degradation ($\gamma = 0$), in addition to the two above, there are infinitely many “intermediate” spatially homogeneous steady states ($0 < \bar{n}, \bar{\rho} < 1$ with $\bar{n} + \bar{\rho} = 1$). All these steady states are stable to both spatially homogeneous and inhomogeneous perturbations, partly due to the fact that they all satisfy volume filling conditions, close to which various dynamics are hindered by saturation effects.

In the absence of saturation effects, we obtain the same spatially homogeneous steady states, which are stable to spatially homogeneous perturbations, but may be unstable to spatially inhomogeneous perturbations thanks to chemotaxis (high χ and/or α_c) and cell-to-cell adhesion (high S_{nn}), given $\bar{n} > 0$ is large enough. This suggests patterns may arise when employing initial conditions that are far from being volume filling, so that cell-to-cell adhesions and chemotaxis may play a significant role: we therefore consider the initial ECM density in (11) to be $\rho_0 = 0.5$ for the simulations of the nondimensional model under the baseline parameter set.

We note that these observations are in line with the existence of a critical initial density for vascular networks to form, as previous pattern formation studies have often concluded that too low or too high initial cell densities will not allow for spatially inhomogeneous perturbations to grow – *vid.* for instance [3] and references therein.

3.2 Cluster formation under the baseline parameter set

We report in Figure 3 the cell density $n(t, x)$ obtained from numerical simulations of the 1D model under the baseline parameter set and in Figure 4 the corresponding cluster width W and compactness C measured. The plots displayed in these figures indicate that our model predicts three stages of cluster formation in 1D. First EPCs form aggregates which reach minimum cluster width of about $W = 0.2$ around $t = 17$ (*cf.* left panel in Figure 3 and Figure 4). Then the cells in these aggregates continue to proliferate increasing their compactness while keeping the cluster width unchanged up to about $t = 50$ (*cf.* central panel in Figure 3 and Figure 4). Finally, the cells continue to proliferate until the whole domain is occupied by cells (*cf.* right panel in Figure 3 and Figure 4).

The simulated dynamics of cluster formation nicely match the experimentally observed ones by Blatchley *et al.* [12], although in our simulations they occur on a slightly slower timescale. In fact in [12] the minimum cluster size was reached around 24 hours (about nondimensional time $t = 8.7$) and kept unchanged while clusters increased compactness up to 48 hours ($t = 17.3$) before late stage dynamics kick in. The numerically obtained cluster width corresponds to about $200 \mu\text{m}$, which perfectly falls in the range of cluster diameters observed in [12]. Finally, after $t = 50$ we observe the equivalent of whole tissue invasion, suggesting our modelling framework cannot properly capture cluster stabilisation in the long run, at least in the 1D case.

3.3 Qualitative investigation of the determinants of cluster formation

In view of the results reported in Section 3.2, we now investigate the role played by chemotaxis, matrix degradation and cell-to-cell adhesion in cluster formation by varying the relevant parameter values and observing changes in the solution up until $t = 50$, starting from the same initial conditions considered in the previous section.

The role of chemotaxis and matrix degradation The plots reported in the second row of Figure 5 reveal the role of chemotaxis and matrix degradation in cluster formation, according to the dynamics described in Section 2.1. Under the baseline parameter set we observe cluster formation (*cf.* first plot in second row of Figure 5), as discussed in the previous paragraph and summarised in Figure 3. In absence of matrix degradation, even though cell aggregates of the same width form, these occupy a fraction of the local volume too small – here $n(t, x) < 0.3$ for all $(t, x) \in (0, \infty) \times \Omega$ – to be considered clusters (*cf.* second plot in second row of Figure 5). On the other hand, in absence of chemotaxis no cell aggregation occurs and we either observe total invasion

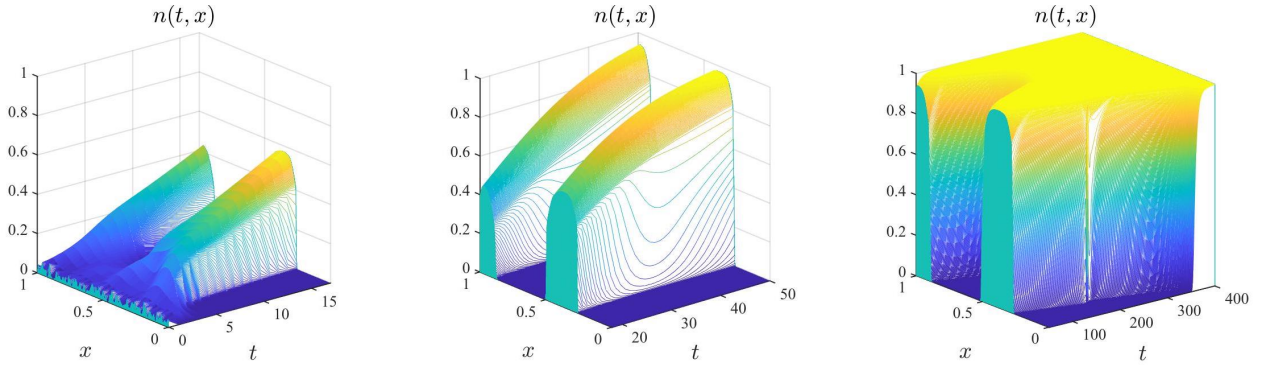


Figure 3: Plots of the cell density $n(t, x)$ obtained solving the system (13), together with definitions (4), (6) and (14), initial conditions (11) and (12)₁, complemented with zero Neumann boundary conditions, under the baseline parameter set in Table 1. The solution is plotted in the time intervals $t = [0, 17]$ (left panel), $t = [17, 50]$ (central panel) and $t = [50, 400]$ (right panel).

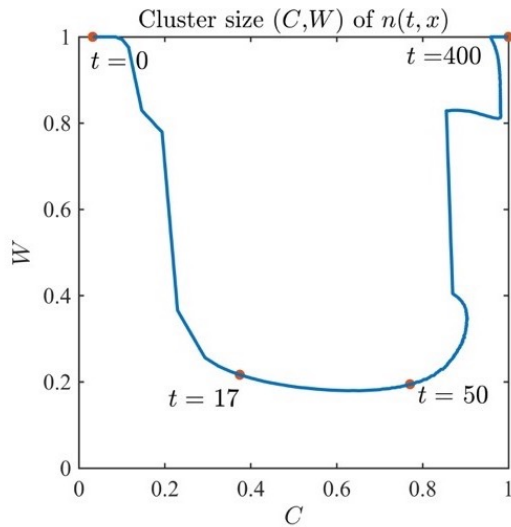


Figure 4: Average cluster width W (19) and cluster compactness C (20) (left panel) measured over time on the cell density $n(t, x)$ (right panel) obtained solving the system (13), together with definitions (4), (6) and (14), initial conditions (11) and (12)₁, complemented with zero Neumann boundary conditions, under the baseline parameter set in Table 1, reported in Figure 3.

of the domain by the cells (*cf.* third plot in second row of Figure 5) or, in absence of matrix degradation, a simple spatial redistribution of the cells (*cf.* fourth plot in second row of Figure 5). These results indicate that chemotaxis and matrix degradation are both crucial to cluster formation, with chemotaxis playing a key role in cell aggregation and matrix degradation being responsible for these aggregates to grow into well-defined and compact clusters.

The role of cell-to-cell adhesion A comparison of the plots in the second row of Figure 5 with those in the rest of the figure reveals the role of cell-to-cell adhesion in cluster formation. These, in fact, have been obtained by varying the cell-to-cell adhesion coefficient S_{nn} , the value of which was chosen *a priori* due to lack of proper estimates in the current literature. We immediately observe that, under the baseline parameter set, cell-to-cell adhesion does not play any particular role in cluster formation, as demonstrated by the fact that the simulations in absence of cell-to-cell adhesion perfectly mirror those with $S_{nn} = 0.1$ (*cf.* first and second row of Figure 5). On the other hand, increasing the order of magnitude of the cell-to-cell adhesion coefficient results in the formation of small-scale aggregates. For $S_{nn} = 1$, these then merge into larger clusters in presence of chemotaxis (*cf.* first and third plot in the third row of Figure 5), while for $S_{nn} = 10$ cell-to-cell adhesion dynamics overpower chemotaxis (*cf.* first and third plot in the fourth row of Figure 5). Finally, independently of the strength of cell-to-cell adhesion, it is evident from Figure 5 that matrix degradation is responsible for cell aggregates to grow above the threshold value of 0.5 (*cf.* first and third columns *vs* second and fourth columns in Figure 5). These results support the hypothesis that chemotaxis and matrix degradation are crucial for cluster formation, while cell-to-cell adhesion is prevalently responsible for cluster stabilisation.

3.4 Quantitative investigation of the determinants of cluster size

We study changes in the measures W and C , defined according to (19) and (20), at $t = 50$ under variations of each parameter in the baseline parameter set. In particular, we consider the effect of halving and doubling the magnitude of each parameter in equations (13)₁ and (13)₂ in Figure 6, and those in equations (13)₃ and (13)₄ in Figure 7. Each boxplot had been obtained using data from 100 simulations under the same parameter set, starting from randomised initial conditions as in (11) and (12)₁.

The cluster width W measured over 100 simulations under the baseline parameter width ranges between 0.15 and 0.41 with median (and mean) around 0.23, as portrayed in Figures 6 and 7 (central boxplot in each W plot). This nondimensional width corresponds to a diameter in the range $150 - 410\mu\text{m}$, which agrees with the experimentally observed clusters' size in [12] (*vid.* for instance Figure 1A or Figure 4C in [12]).

The role of chemotaxis Boxplots of the width W and compactness C of clusters for different values of the chemotactic sensitivity χ are displayed in Figure 6b. While higher values of χ correlate with slightly smaller clusters, yet maintaining a mean width around 0.2, lowering the magnitude of χ seems to result in a wider range of values of W with much higher median, as well as higher compactness C . This supports the notion that lowering the chemotactic sensitivity of the cells hinders cluster formation and – assuming all other dynamics are present – fosters tissue invasion, which is in line with the results presented in Section 3.3.

The role of VEGFs dynamics Figure 7e displays changes in clusters' width W and compactness C as the rate production of VEGFs α_c varies. Note that these results well mirror those obtained by varying chemotactic sensitivity (*cf.* Figure 6b and 7e), which is coherent with the notion that higher VEGF production rates correlate with stronger chemotactic dynamics, already established to play a key role in cluster formation. Recall that we expect α_c to be reflective of the local level of hypoxia: in this perspective, our results well match the experimental ones of Akita and coworkers [1], whereby clusters only formed under hypoxic conditions and not in normoxic ones. In addition, the size of clusters seems to be proportional to the VEGF diffusion coefficient D_c , as demonstrated by the plots in Figure 7d in which we see that increasing the magnitude of D_c results in higher W and C . This trend, however, suggests that much higher values of D_c may result in tissue invasion, rather than cluster formation (see supplementary Figure S1a in 'SuppInfo' document). Finally, as suggested by Figure 7f, changes in the VEGF decay rate λ_c do not seem to particularly effect clusters' size.

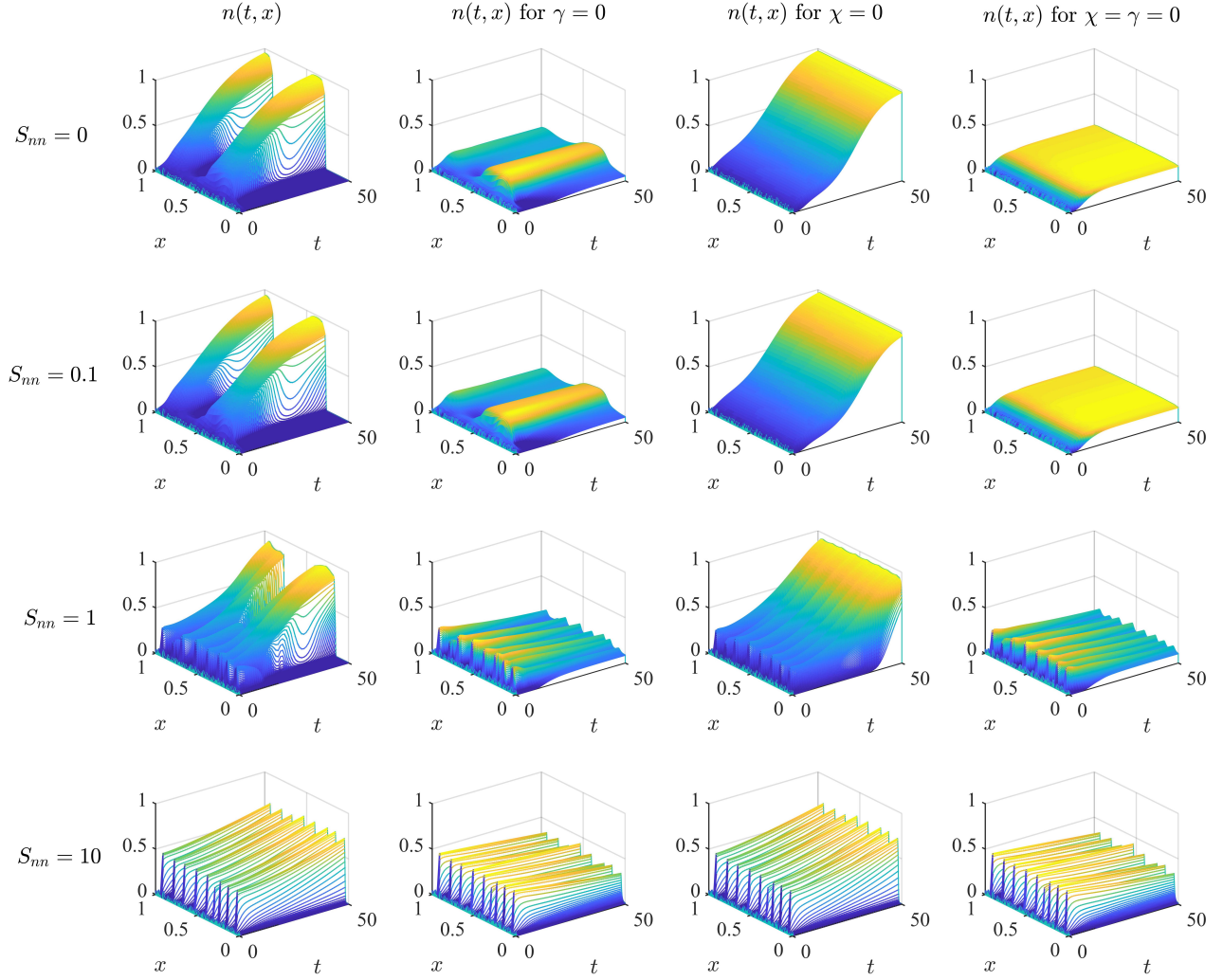


Figure 5: **First row:** Plots of the cell density $n(t, x)$ up to $t = 50$ obtained solving the system (13), together with definitions (4), (6) and (14), initial conditions (11) and (12)₁, complemented with zero Neumann boundary conditions, in absence of cell-to-cell adhesion, *i.e.* for $S_{nn} = 0$: under the baseline parameter set (first column), in absence of matrix degradation, *i.e.* for $\gamma = 0$ (second column), in absence of chemotaxis, *i.e.* $\chi = 0$ (third column), and in absence of both chemotaxis and matrix degradation, *i.e.* $\chi = \gamma = 0$ (fourth column). **Second, third and fourth rows:** Same as first row but in the presence of cell-to-cell adhesion, with $S_{nn} = 0.1$ (second row), $S_{nn} = 1$ (third row) and $S_{nn} = 10$ (fourth row) respectively.

The role of matrix degradation Boxplots of the width W and compactness C of clusters for different values of the matrix degradation rate γ are displayed in Figure 6f. Notice that, while the median width W is maintained around 0.2, increasing the magnitude of γ results in a smaller range of values measured for both W and C , as well as higher values of cluster compactness. In addition, this trend suggests that further decreasing γ will lead to higher values of W and lower values of C measured (see supplementary Figure S1b in ‘SuppInfo’

document), which is in line with the observed dynamics in absence of matrix degradation in Section 3.3 (*cf.* Figure 5, second and fourth columns). Overall, this highlights the key role matrix degradation has in cluster formation, establishing a relation between the rate γ and the clusters' compactness C .

The role of MMPs dynamics Figure 7b displays changes in clusters' width W and compactness C as the rate production of MMPs α_m varies. Similarly to what was observed for α_c in relation to χ , we see that these boxplots closely resemble those obtained varying γ (*cf.* Figures 6f and 7b), which is coherent with the notion that higher MMP production rates correlate with stronger degrading dynamics, already established to be responsible for turning aggregates into clusters – that is, increasing their compactness. Recall that we expect α_m to be reflective of the local level of hypoxia: in this perspective, our results well match the experimental ones of Blatchley and coworkers [12], whereby higher levels of hypoxia correlate with better defined clusters. In addition, we see in Figure 7c that increasing the magnitude of the MMPs decay rate λ_m yields opposite effects to those obtained increasing their production α_m , further confirming the role MMP-mediated matrix degradation has in cluster formation. On the other hand, changes in the MMPs diffusivity D_m do not seem to affect clusters' size, as demonstrated in Figure 7a – verified under different orders of magnitude of D_m (see supplementary Figure S1c in ‘SuppInfo’ document). This suggests not much will be gained by distinguishing between membrane-bound and diffusive MMPs, at least in this modelling framework.

The role of matrix remodelling We see in Figure 6g that increasing the magnitude of the matrix remodelling rate μ yields opposite effects to those obtained increasing its degradation rate γ (*vid.* Figure 6f), which is coherent with the opposite nature of these dynamics.

The role of cell-to-cell adhesion The plots in Figure 6c confirm that small variations in the cell-to-cell adhesion coefficient S_{nn} do not influence the size of clusters, as expected from the results in Section 3.3. Additional numerical tests considering different orders of magnitude of S_{nn} (see supplementary Figure S1d in ‘SuppInfo’ document) revealed a slight increase in the median W , probably due to the initial presence of smaller clusters (*cf.* Figure 5, third row) which at $t = 50$ may still be in the process of merging depending on their spatial distribution. Overall, this excludes cell-to-cell adhesion from the list of key parameters in determining cluster – and therefore network – topology.

The role of cell diffusion and cell-matrix interactions The boxplots of W and C of clusters for different values of the cell diffusion coefficient D_n , displayed in Figure 6a, show that changing the magnitude of D_n has very little effect on the clusters' compactness C and median width W . There is however an increasing range of values of W measured as D_n increases, indicating that low diffusivity correlates with more precisely defined clusters, while high diffusivity results in more variability in cluster size. Moreover, this variability allows for larger values of W to be measured, suggesting that much higher diffusivity may result in tissue invasion (see supplementary Figure S1e in ‘SuppInfo’ document). The same observations can be conducted on the boxplots in Figure 6d, obtained by varying the magnitude of the cell-to-matrix adhesion coefficient. This is in line with the notion that lower cell-matrix interactions facilitate cluster formation, while much higher cell-matrix interactions promote tissue invasion.

The role of cell proliferation In Figure 6e we see that slower proliferation – *i.e.* lower p – correlates with a wide range of lower values of cluster compactness C measured, while the median width is maintained around 0.2. On the other hand, faster proliferation – *i.e.* higher p – results in a wide range of higher values of cluster width W and a small range of high values of compactness C . Note that these data portray different stages of the cluster formation process, as demonstrated in Figure 4 (central panel): initially aggregates form without being very condensed (low-to-medium W and C), then they increase their compactness while keeping steady

width (low W and high C), and eventually grow further invading the surrounding space (medium-to-high W and high C). This suggests that the rate of proliferation of EPCs might play a key role in determining the speed of the cluster formation process.

The role of initial ECM density The plots in Figure 6h indicate that changes in the initial ECM density ρ_0 does not affect the overall spatio-temporal dynamics. In fact, while different values of ρ_0 results in slightly different values of the median width and compactness of clusters observed at $t = 50$, these values still capture the same biological scenario (*i.e.* cluster are recognisable at $t = 50$).

3.5 Two-dimensional clusters

Let us now consider the 2D problem. In this section we focus on the most interesting results obtained in Section 3.4 and investigate the role played by chemotaxis, matrix degradation and cell proliferation in the formation of 2D clusters.

2D clusters under the baseline parameter set Under the baseline parameter set reported in Table 1, 2D cluster formation follows slightly different spatio-temporal dynamics to those observed in the 1D case, as demonstrated by the plots in the second row of Figures 8, 9 and 10. At $t = 20$ the cell density has already reached maximum local compactness in some regions, while aggregation dynamics are still at their early stages (*cf.* first panel in second row of Figures 8, 9 or 10), and the minimum cluster size is observed no earlier than $t = 140$ (*cf.* forth panel in second row of Figures 8, 9 or 10). The cluster observed at this stage has a nondimensional diameter of about 0.2, which perfectly agrees with the results in 1D and is therefore coherent with experimental observations reported by Blatchley *et al.* [12]. After the cluster has formed, no tissue invasion is observed – see supplementary Figure S2 in ‘SuppInfo’ document.

The role of matrix degradation The plots reported in Figure 8 demonstrate that matrix degradation promotes the formation of 2D clusters, as predicted by the results of the 1D model presented in Sections 3.3 and 3.4. Lower matrix degradation rates correlate with slower aggregation dynamics and lower compactness of such aggregates (*cf.* first row of Figure 8) – to the extent that in absence of matrix degradation no clusters form (see supplementary Figure S3 in ‘SuppInfo’ document) – and higher matrix degradation rates correlate with faster cluster formation with well-defined and compact clusters observed at much earlier times (*cf.* third row of Figure 8). We obtain the same results under analogous variations of the MMP secretion rate α_m (see supplementary Figure S4 in ‘SuppInfo’ document), assumed to be related to the level of hypoxia, which well agrees with the experimental results by Blatchley and coworkers [12], whereby higher levels of hypoxia correlate with better defined clusters.

The role of chemotaxis The plots reported in Figure 9 demonstrate that endogenous chemotaxis promotes aggregation dynamics, as predicted by the results of the 1D model presented in Sections 3.3 and 3.4, and reveal that chemotaxis is an important determinant of 2D cluster topology. Lower values of the chemotactic sensitivity χ correlate with slower and weaker aggregation dynamics, so that no well-defined clusters can be observed (*cf.* first row of Figure 9). Higher values of χ correlate with faster and stronger aggregation dynamics, with well-defined clusters observed at earlier times (*cf.* third row of Figure 9) and cluster diameter – once the clusters have reached minimum size – smaller than that observed with lower values of χ (*cf.* last panel in the second row and last panel in the third row of Figure 9). We obtain the same results under analogous variations of the VEGF secretion rate α_c (see supplementary Figure S5 in ‘SuppInfo’ document), assumed to be related to the level of hypoxia, which well agrees with the experimental results by Akita and coworkers [1], whereby hypoxia-preconditioned cells formed better defined clusters.

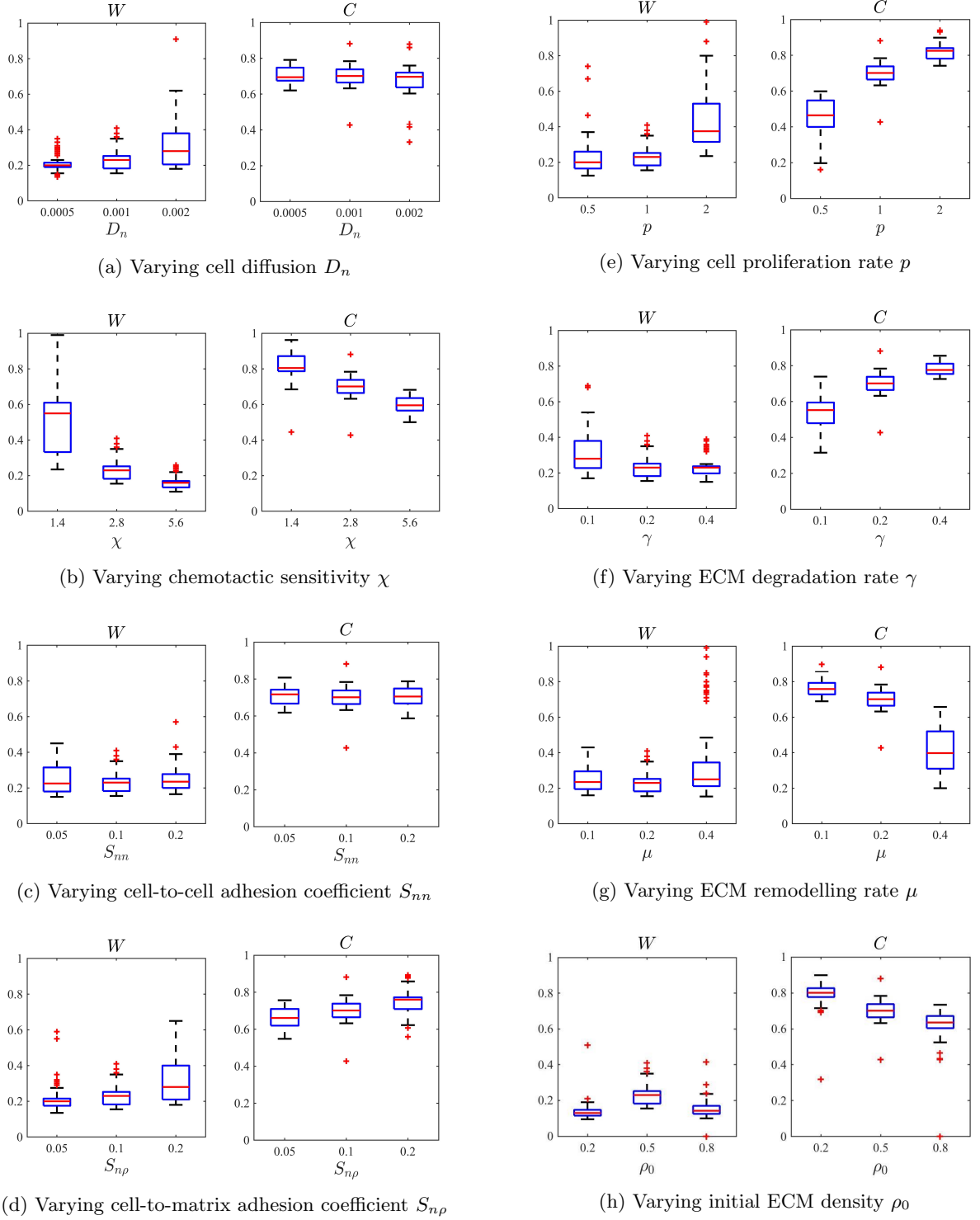


Figure 6: Cluster width W and compactness C , defined in (19) and (20), under variations from the baseline parameter set (BPS), in Table 1, of each parameter in equations (13)₁ and (13)₂. In (a) we have boxplots of W and C measured on the numerical solution of the system (13) at $t = 50$, for D_n taking its value in the BPS (center), half (left) and double (right) its value in the BPS. Each boxplot collects data from 100 simulations under randomised initial conditions (11)-(12)₁. In (b)-(g) we have the same as in (a) but varying parameters χ (b), S_{nn} (c), $S_{n\rho}$ (d), p (e), γ (f), μ (g) and ρ_0 (h). 17

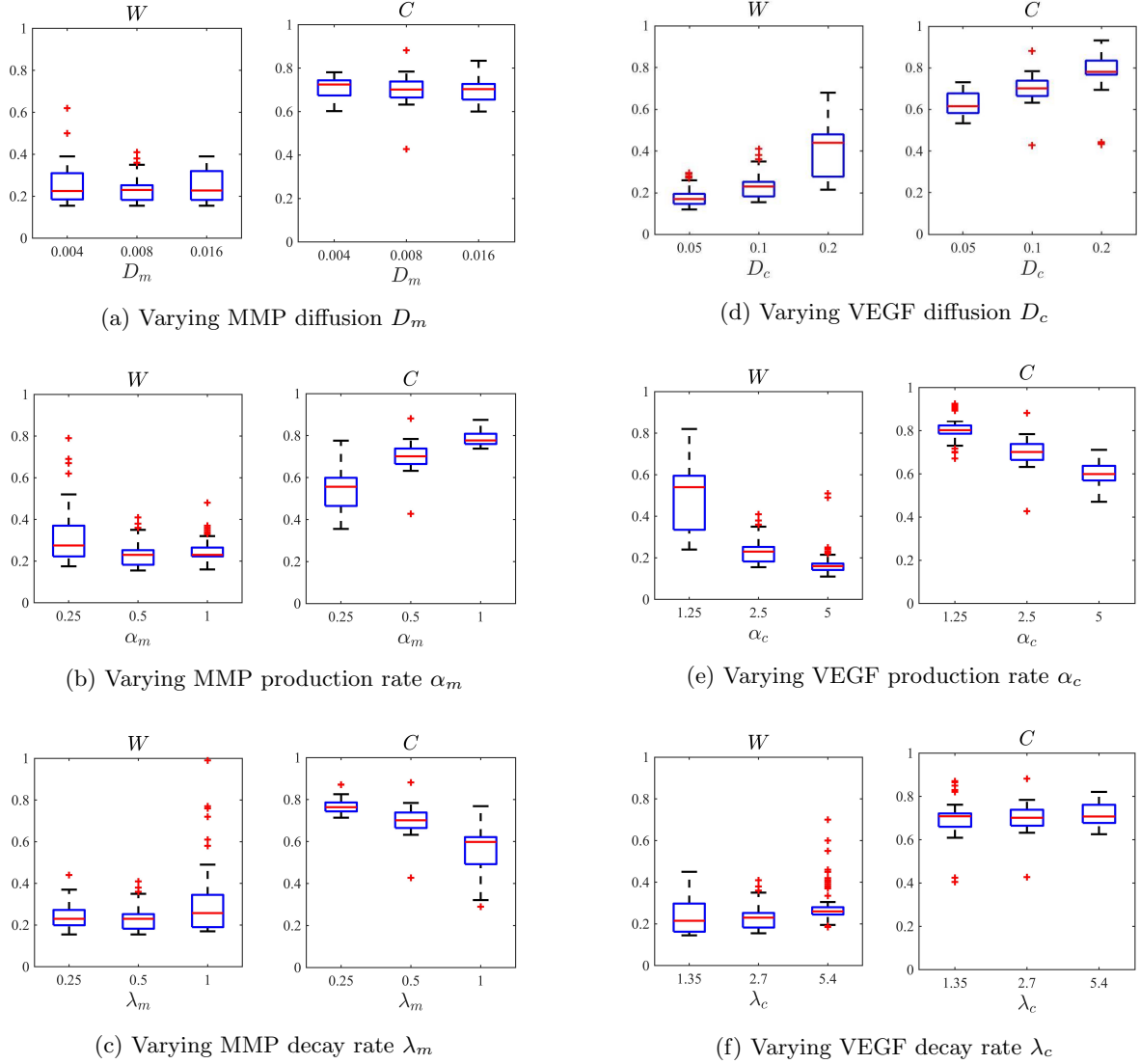


Figure 7: Cluster width W and compactness C , defined in (19) and (20), under variations from the baseline parameter set in Table 1 of each parameter in equations (13)₃ and (13)₄. In (a) we have boxplots of W and C measured on the numerical solution of the system (13) at $t = 50$, for D_m taking its value in the BPS (center), half (left) and double (right) its value in the BPS. Each boxplot collects data from 100 simulations under randomised initial conditions (11)-(12)₁. In (b)-(f) we have the same as in (a) but varying parameters α_m (b), λ_m (c), D_c (d), α_c (e) and λ_c (f).

The role of cell proliferation While the results of the 1D model presented in Section 3.4 suggested that the speed of the cluster formation process was proportional to the cell proliferation rate p , the plots reported in Figure 10 indicate that this may not be the case in a 2D framework. While the rate of cell proliferation may influence how the cells respond to spatial gradients at the beginning of the cluster formation process (*cf.* plots in the second column of Figure 10), it does not seem affect the overall spatio-temporal dynamics of 2D cluster formation. Upon these considerations, the results displayed in Figure 6e may simply be a 1D projection of the

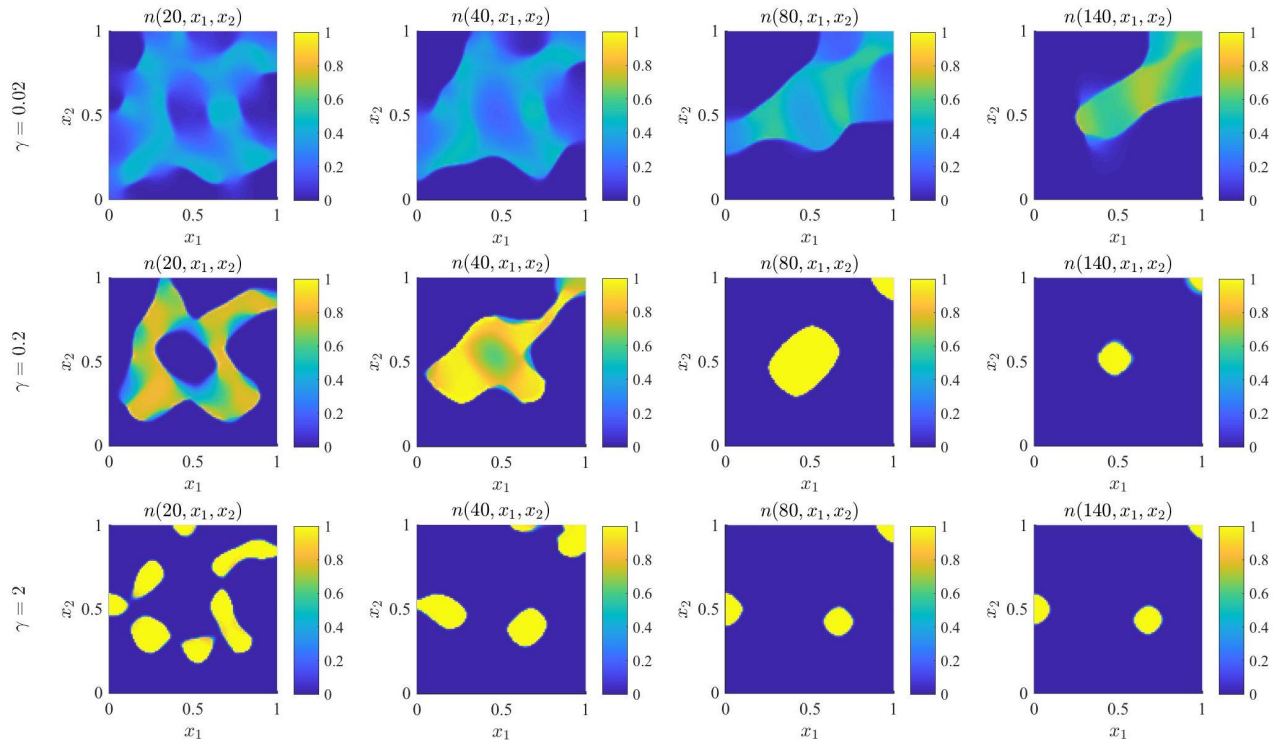


Figure 8: **First row:** Plots of the cell density $n(t, x)$ obtained solving the system (13), together with definitions (5), (6) and (14), initial conditions (11) and (12)₂, complemented with zero Neumann boundary conditions, under the parameter choices reported in Table 1, except for $\gamma = 0.02$. The solution is plotted at time $t = 20$ (first panel), $t = 40$ (second panel), $t = 80$ (third panel) and $t = 140$ (fourth panel). **Second and third row:** Same as first row, except for $\gamma = 0.2$ (second row) and $\gamma = 2$ (third row).

2D dynamics occurring around the same time – consider for instance a 1D cross section (*e.g.* $x_1 = 0.5$) of the plots in the second column of Figure 10.

4 Conclusions and research perspectives

Despite the great progress made in the past 20 years in understanding the mechanisms behind EPC cluster-based vasculogenesis, much more needs to be achieved in order to unlock its full therapeutic potential. Mathematical modelling provides theoretical means to shed light on the otherwise hidden role played by underlying dynamics in the origin and structure of the emergent vascular network, as previously achieved in the study of mature EC vascular network formation (single-cell vasculogenesis). We therefore formulated a mathematical model of EPC cluster formation during the early stages of vasculogenesis, including mechanisms such as matrix degradation, cell proliferation and cell-to-cell adhesion, which were found to distinguish cluster-based vasculogenesis from single cell vasculogenesis. Thanks to the introduction of appropriate metrics of cluster width and compactness, we investigated the role played by underlying dynamics in facilitating cluster formation, regulating the speed of the cluster-formation process and the size of clusters, verifying the key results of the 1D model still held in a 2D framework.

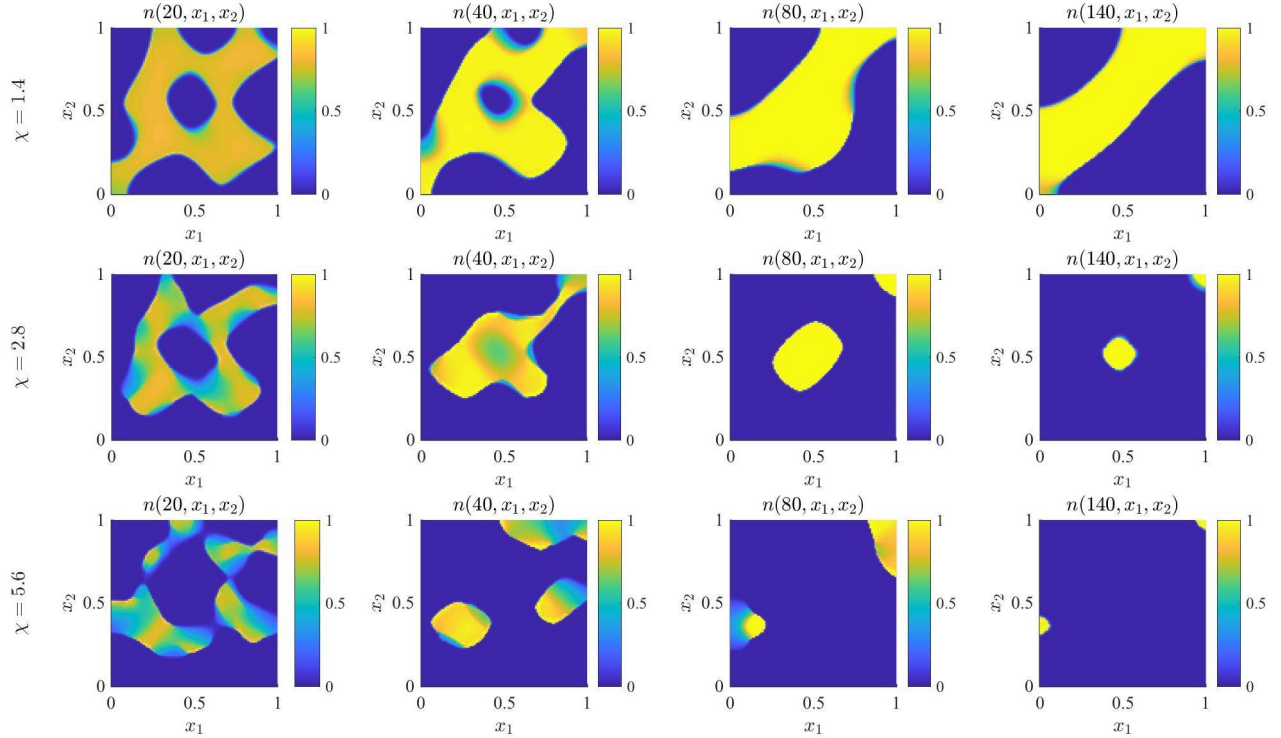


Figure 9: **First row:** Plots of the cell density $n(t, x)$ obtained solving the system (13), together with definitions (5), (6) and (14), initial conditions (11) and (12)₂, complemented with zero Neumann boundary conditions, under the parameter choices reported in Table 1, except for $\chi = 1.4$. The solution is plotted at time $t = 20$ (first panel), $t = 40$ (second panel), $t = 80$ (third panel) and $t = 140$ (fourth panel). **Second and third row:** Same as first row, except for $\chi = 2.8$ (second row) and $\chi = 5.6$ (third row).

Our results confirmed the role played by matrix degradation, assumed to be correlated with the level of hypoxia, in the formation of EPC clusters both with the 1D and 2D models, providing additional theoretical support to the mechanism of EPC cluster formation proposed by Blatchley *et al.* [12]. In addition, the investigation conducted in Sections 3.4 and 3.5 indicates that the speed of cluster formation is proportional to the rate of matrix degradation – or the rate of MMP secretion by the cells – which nicely agrees their experimental observations. Our numerical results further highlighted that matrix degradation alone may not suffice to explain the formation of clusters, as endogenous chemotaxis was shown to be responsible for aggregation dynamics, without which the cells would simply invade the whole tissue. In addition, the investigation conducted in Sections 3.4 and 3.5 suggests that the size of clusters is (inversely) related to the chemotactic sensitivity of the cells, indicating chemotaxis may be a key determinant of cluster – and network – topology.

While the role played by matrix degradation and the size of clusters in our numerical simulations well matches the experimental observations reported by Blatchley and coworkers [12], this – and future – mathematical models would benefit from the estimation of parameter values by fitting the model to experimental data in order to obtain a better match of the timescale of 2D cluster formation. This could be achieved, for instance, by considering increased values of the MMP and VEGF production rates (α_m and α_c), which has been observed in hypoxic environments [1, 12]. We also note that the ten-fold increase in α_m which results in the observation

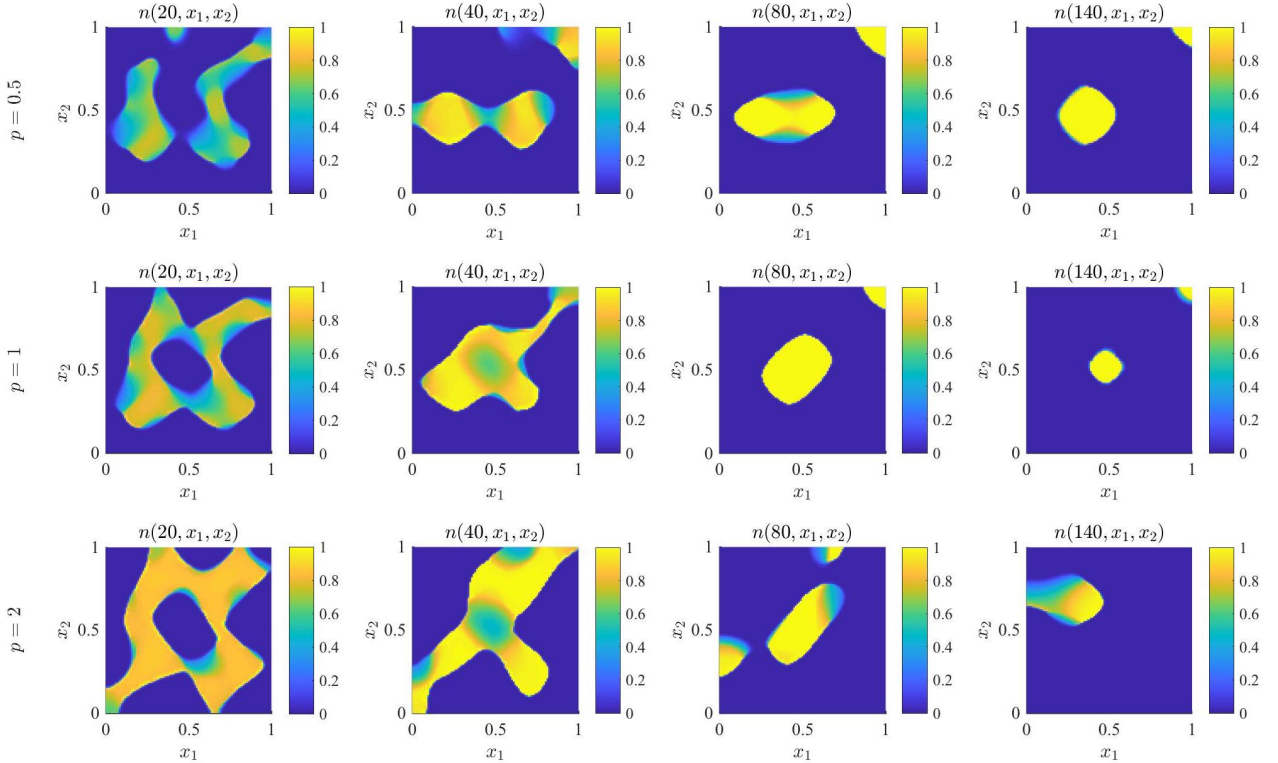


Figure 10: **First row:** Plots of the cell density $n(t, x)$ obtained solving the system (13), together with definitions (5), (6) and (14), initial conditions (11) and (12)₂, complemented with zero Neumann boundary conditions, under the parameter choices reported in Table 1, except for $p = 0.5$. The solution is plotted at time $t = 20$ (first panel), $t = 40$ (second panel), $t = 80$ (third panel) and $t = 140$ (fourth panel). **Second and third row:** Same as first row, except for $p = 1$ (second row) and $p = 2$ (third row).

of well-defined clusters at $t = 20$ (see supplementary Figure S4) is justified by the experimental conditions reported in [12].

The mathematical study of cluster-based vasculogenesis would also benefit from a more suited description of cell-to-cell adhesion, as we have seen in Section 3.3 that our modelling choice allows us to capture the aggregative effect of cell-to-cell adhesion, but not its role in cluster stabilisation. This could be more easily achieved by adopting an individual-based or hybrid modelling approach [5, 60, 66, 67], as done in previous single-cell vasculogenesis works [38, 54, 53, 62]. Moreover, given previous results of PEC models of single-cell vasculogenesis [4, 3, 22, 56], it would be interesting to investigate whether clusters would still form in this modelling framework with the inclusion of persistence of motion.

We plan to extend the theoretical investigation of cluster-based vasculogenesis to later stages of this process, during which EPCs increase their interaction with the ECM and bridge clusters, forming the vascular network. At such stage the mechanical interaction between the cells and ECM becomes non-trivial and we are therefore going to consider a mechanochemical model similar to those previously proposed to study the late stages of single-cell vasculogenesis [37, 41, 65]. Upon formulation of a mathematical model which accurately predicts

vascular network assembly, this could be used to investigate the determinants of network size and topology, exploring for instance whether the size of clusters will affect tube diameters or whether VEGF diffusion and decay rates determine chord length as suggested for single-cell vasculogenesis [4, 3, 22, 56], and how these are affected by matrix stiffness.

Conflict of interest

The authors declare that they have no conflict of interest.

A Parameter values

As already indicated in Section 2.2, we use $L = 0.1$ cm as characteristic length scale, in accordance with previous vasculogenesis works [37, 56] and for easy visual comparison with the experimental results reported by Blatchley and coworkers [12]. We then take reference time scale $\tau := L^2/D$, where D is a characteristic diffusion coefficient $D \sim 10^{-6}$ cm²s⁻¹ [13], resulting in a reference time scale $\tau = 10^4$ s.

Endothelial progenitor cells (or endothelial cells) The reference cell density is chosen to be $N := n_M = \vartheta_1^{-1}$ and we take ϑ_1 to be the average volume occupied by an EC. Rubin and coworkers [49] measured the average ECs volume during different phases of the cell cycle, registering values in the range of 800 – 1800 μm^3 , with a predominance of measurements around 1000 μm^3 . Hence we take $\vartheta_1 = 10^{-9}$ cm³/cell, corresponding to an average cell diameter of approximately $a = 10^{-3}$ cm. Measures and estimates of the diffusion coefficient of ECs fall in the range 10^{-6} - 10^{-12} cm²s⁻¹ [3], so we take $D_n = 10^{-9}$ cm²s⁻¹. We consider the chemotactic sensitivity coefficient estimated by Jain and Jackson [28], corresponding to $\chi = 1.4 \times 10^{-7}$ cm⁵ng⁻¹s⁻¹. Sen *et al.* [55] estimated a maximum cell surface radius, upon morphological changes to better adhere to the underlying gel, of about 50 μm . Given cell-to-cell and cell-to-matrix adhesion occurs via adhesion molecules on the cell surface, we take the sensing radius $R = 0.5 \times 10^{-2}$ cm. While the nonlocal term introduced in equations (4) and (5) allows us to well consider cell-to-cell and cell-to-matrix adhesion dynamics at tissue level, these are the result of smaller scale dynamics between adhesion molecules and receptors on cell surfaces – *vid.* for instance [2, 11, 23] – of which our modelling choice is a simplification. As a result, good estimates for cell-to-cell and cell-to-matrix coefficients S_{nn} and $S_{n\rho}$ are currently lacking. We therefore consider nondimensional values chosen in [25] for our baseline parameter set which correspond to $S_{nn} = 10^{-16}$ cm⁵ s⁻¹ and $S_{n\rho} = 10^{-6}$ cm² nM⁻¹ s⁻¹ respectively, acknowledging that model fitting to experimental data is required. Kinev and coworkers [31] reported doubling times of non-irradiated ECFCs – the same class of EPCs employed by Blatchley *et al.* [12] – of about 19.5 hours, estimated from measured growth rates assuming exponential growth. Following their calculations, this corresponds to proliferation rates of about $p = 10^{-5}$ s⁻¹.

Extracellular matrix We use a reference matrix density of $P = 10^{-1}$ nM [5, 6, 64] and define the parameter $\vartheta_2 := P^{-1}$. We take the matrix degradation rate by MMPs proposed by Kim and Friedman [30], *i.e.* $\gamma = 9 \times 10^5$ cm³g⁻¹s⁻¹. ECM remodelling is a complex process involving a variety of cells and molecules [15, 18, 36, 61], so the remodelling term introduced in equation (8) is an oversimplification of the underlying dynamics. Therefore the lack of experimental values or estimates for the remodelling rate μ is not surprising, and we take the nondimensional value 0.2 as similarly considered in [19, 21, 25] for our baseline parameter set. Under the defined nondimensional parameters this corresponds to the dimensional value $\mu = 0.2 \times 10^{-5}$ nM s⁻¹.

Matrix degrading enzyme (MMP) Blatchley *et al.* [12] reported concentrations of MMP-1 in the range 1 – 100 $\mu\text{g ml}^{-1}$, so we take the intermediate concentration as reference MMP density, *i.e.* $M = 10$ $\mu\text{g cm}^{-3}$.

We let the diffusion coefficient for the MMP be given by $D_m = 8 \times 10^{-9} \text{ cm}^2\text{s}^{-1}$, which was experimentally determined by Saffarian and coworkers [52], although diffusion rates have been observed in the range $10^{-10} - 10^{-8} \text{ cm}^2\text{s}^{-1}$ [16, 34]. While MMPs secretion rates by cells have been reported in a variety of works, these fail to provide parameter values in the appropriate unit of α_m in this model. For instance in [34] secretion rates considered varying between $0.01 - 0.5 \text{ s}^{-1}$ but the associated MMP concentration is unspecified, while in [50] the estimated rate is of 5.75×10^{-10} and $4.44 \times 10^{-10} \text{ g cm}^{-3}$ secreted by stromal cells and macrophages respectively, without an indication of the considered time frame. We therefore here consider that molecular dynamics are generally faster than cellular ones and therefore the observed average MMP concentration satisfies (9) at equilibrium, *i.e.* $m = \alpha_m n / \lambda_m$. Under the chosen reference values N , M and λ_m , this corresponds to an MMP production rate of $\alpha_m = 0.5 \times 10^{-12} \mu\text{g s}^{-1}$ per cell. Note that the resulting nondimensional parameter value is close to those chosen in previous mathematical models – *vid.* for instance [6, 19, 21, 25]. Nonetheless, we will also consider higher values of α_m , since Deem and Cook-Mills [20] have reported up to a 4-fold increase in MMP production in the presence of ROS, and in addition MMP production levels have been shown to be significantly upregulated in human cancers [59]. Finally, Kim and Friedman [30] estimated – from its half life – the decay rate of MMP $\lambda_m = 5 \times 10^{-5} \text{ s}^{-1}$.

Chemoattractant (VEGF) We take the reference VEGF density to be $C = 20 \text{ ng cm}^{-3}$, in the range of values generally considered in *in vitro* set ups – *vid.* for instance [26, 35, 56]. Measures and estimates of the diffusion coefficient of the chemoattractant, usually identified as VEGF, are in the range $10^{-6} - 10^{-9} \text{ cm}^2\text{s}^{-1}$ [3, 22, 38, 39, 56, 60], so we take $D_c = 10^{-7} \text{ cm}^2\text{s}^{-1}$. Yen and coworkers [70] reported a VEGF secretion rate of $0.068 \text{ molecules cell}^{-1}\text{s}^{-1}$, which in combination with Avogadro’s number (6.022×10^{23} molecules per mole) and a molecular weight of 45kDa [70] results in a VEGF production rate of about $\alpha_c = 0.5 \times 10^{-11} \text{ ng s}^{-1}$ per cell. Serini *et al.* [56] reported the half-life of VEGF-A to be approximately 64 minutes, corresponding to a decay rate of about $\lambda_c = 2.7 \times 10^{-4} \text{ s}^{-1}$, in line with the values chosen in [38, 60].

References

- [1] T. AKITA, T. MUROHARA, H. IKEDA, K.-I. SASAKI, T. SHIMADA, K. EGAMI, AND T. IMAIZUMI, *Hypoxic preconditioning augments efficacy of human endothelial progenitor cells for therapeutic neovascularization*, Laboratory Investigation, 83 (2003), pp. 65–73.
- [2] S. M. ALBELDA AND C. A. BUCK, *Integrins and other cell adhesion molecules*, The FASEB Journal, 4 (1990), pp. 2868–2880.
- [3] D. AMBROSI, F. BUSSOLINO, AND L. PREZIOSI, *A review of vasculogenesis models*, Journal of Theoretical Medicine, 6 (2005), pp. 1–19.
- [4] D. AMBROSI, A. GAMBA, AND G. SERINI, *Cell directional and chemotaxis in vascular morphogenesis*, Bulletin of Mathematical Biology, 66 (2004), pp. 1851–1873.
- [5] A. R. A. ANDERSON, *A hybrid mathematical model of solid tumour invasion: the importance of cell adhesion*, Mathematical Medicine and Biology, 22 (2005), pp. 163–186.
- [6] A. R. A. ANDERSON, M. A. J. CHAPLAIN, E. L. NEWMAN, R. J. C. STEELE, AND A. M. THOMPSON, *Mathematical Modelling of Tumour Invasion and Metastasis*, Journal of Theoretical Medicine, 2 (2000), pp. 129–154.
- [7] N. J. ARMSTRONG, K. J. PAINTER, AND J. A. SHERRATT, *A continuum approach to modelling cell–cell adhesion*, Journal of Theoretical Biology, 243 (2006), pp. 98–113.

- [8] T. ASAHARA AND A. KAWAMOTO, *Endothelial progenitor cells for postnatal vasculogenesis*, American Journal of Physiology-Cell Physiology, 287 (2004), pp. C572—C579.
- [9] T. ASAHARA, H. MASUDA, T. TAKAHASHI, C. KALKA, C. PASTORE, M. SILVER, M. KEARNE, M. MAGNER, AND J. M. ISNER, *Bone marrow origin of endothelial progenitor cells responsible for postnatal vasculogenesis in physiological and pathological neovascularization*, Circulation Research, 85 (1999), pp. 221–228.
- [10] T. ASAHARA, T. MUROHARA, A. SULLIVAN, M. SILVER, R. VAN DER ZEE, T. LI, B. WITZENBICHLER, G. SCHATTEMAN, AND J. M. ISNER, *Isolation of Putative Progenitor Endothelial Cells for Angiogenesis*, Science, 275 (1997), pp. 964–966.
- [11] A. L. BERRIER AND K. M. YAMADA, *Cell–matrix adhesion*, Journal of Cellular Physiology, 213 (2007), pp. 565–573.
- [12] M. R. BLATCHLEY, F. HALL, S. WANG, H. C. PRUITT, AND S. GERECHE, *Hypoxia and matrix viscoelasticity sequentially regulate endothelial progenitor cluster-based vasculogenesis*, Science Advances, 5 (2019), p. eaau7518.
- [13] D. BRAY, *Cell movements: from molecules to motility*, Garland Science, 2000.
- [14] F. BUBBA, C. POUCHOL, N. FERRAND, G. VIDAL, L. ALMEIDA, B. PERTHAME, AND M. SABBAB, *A chemotaxis-based explanation of spheroid formation in 3D cultures of breast cancer cells*, Journal of Theoretical Biology, 479 (2019), pp. 73–80.
- [15] M. CHANG, *Restructuring of the extracellular matrix in diabetic wounds and healing: A perspective*, Pharmacological Research, 107 (2016), pp. 243–248.
- [16] I. E. COLLIER, W. LEGANT, B. MARMER, O. LUBMAN, S. SAFFARIAN, T. WAKATSUKI, E. ELSON, AND G. I. GOLDBERG, *Diffusion of MMPs on the surface of collagen fibrils: the mobile cell surface–collagen substratum interface*, PloS One, 6 (2011), p. e24029.
- [17] A. CONIGLIO, A. DE CANDIA, S. DI TALIA, AND A. GAMBA, *Percolation and burgers’ dynamics in a model of capillary formation*, Physical Review E, 69 (2004), p. 051910.
- [18] W. P. DALEY, S. B. PETERS, AND M. LARSEN, *Extracellular matrix dynamics in development and regenerative medicine*, Journal of Cell Science, 121 (2008), pp. 255–264.
- [19] N. E. DEAKIN AND M. A. J. CHAPLAIN, *Mathematical modeling of cancer invasion: The role of membrane-bound matrix metalloproteinases*, Frontiers in Oncology, 3 (2013), p. 70.
- [20] T. L. DEEM AND J. M. COOK-MILLS, *Vascular cell adhesion molecule 1 (VCAM-1) activation of endothelial cell matrix metalloproteinases: role of reactive oxygen species*, Blood, 104 (2004), pp. 2385–2393.
- [21] P. DOMSCHKE, D. TRUCU, A. GERISCH, AND M. A. J. CHAPLAIN, *Mathematical modelling of cancer invasion: implications of cell adhesion variability for tumour infiltrative growth patterns*, Journal of Theoretical Biology, 361 (2014), pp. 41–60.
- [22] A. GAMBA, D. AMBROSI, A. CONIGLIO, A. DE CANDIA, S. DI TALIA, E. GIRAUDO, G. SERINI, L. PREZIOSI, AND F. BUSSOLINO, *Percolation, morphogenesis, and Burgers dynamics in blood vessels formation*, Physical Review Letters, 90 (2003), p. 118101.
- [23] D. R. GARROD, *Cell to cell and cell to matrix adhesion.*, BMJ: British Medical Journal, 306 (1993), p. 703.

- [24] A. GERISCH, *On the approximation and efficient evaluation of integral terms in PDE models of cell adhesion*, IMA Journal of Numerical Analysis, 30 (2010), pp. 173–194.
- [25] A. GERISCH AND M. A. J. CHAPLAIN, *Mathematical modelling of cancer cell invasion of tissue: local and non-local models and the effect of adhesion*, Journal of Theoretical Biology, 250 (2008), pp. 684–704.
- [26] D. HANJAYA-PUTRA AND S. GERECHT, *Vascular engineering using human embryonic stem cells*, Biotechnology Progress, 25 (2009), pp. 2–9.
- [27] T. HILLEN AND K. J. PAINTER, *Global Existence for a Parabolic Chemotaxis Model with Prevention of Overcrowding*, Advances in Applied Mathematics, 26 (2001), pp. 280–301.
- [28] H. JAIN AND T. JACKSON, *A hybrid model of the role of VEGF binding in endothelial cell migration and capillary formation*, Frontiers in Oncology, 3 (2013), p. 102.
- [29] E. F. KELLER AND L. A. SEGEL, *Initiation of slime mold aggregation viewed as an instability*, Journal of Theoretical Biology, 26 (1970), pp. 399–415.
- [30] Y. KIM AND A. FRIEDMAN, *Interaction of tumor with its micro-environment: A mathematical model*, Bulletin of Mathematical Biology, 72 (2010), pp. 1029–1068.
- [31] A. V. KINEV, V. LEVERING, K. YOUNG, F. ALI-OSMAN, G. A. TRUSKEY, M. W. DEWHIRST, AND D. IL'YASOVA, *Endothelial colony forming cells (ECFCs) as a model for studying effects of low-dose ionizing radiation: growth inhibition by a single dose*, Cancer Investigation, 31 (2013), pp. 359–364.
- [32] D. KOLTE, J. A. MCCLUNG, AND W. S. ARONOW, *Vasculogenesis and Angiogenesis*, in Translational Research in Coronary Artery Disease: Pathophysiology to Treatment, Elsevier Inc., 2016, ch. 6, pp. 49–65.
- [33] R. KOWALCZYK, A. GAMBA, AND L. PREZIOSI, *On the stability of homogeneous solutions to some aggregation models*, Discrete & Continuous Dynamical Systems-B, 4 (2004), p. 203.
- [34] S. KUMAR, A. DAS, A. BARAI, AND S. SEN, *MMP secretion rate and inter-invadopodia spacing collectively govern cancer invasiveness*, Biophysical Journal, 114 (2018), pp. 650–662.
- [35] S. LEE, T. T. CHEN, C. L. BARBER, M. C. JORDAN, J. MURDOCK, S. DESAI, N. FERRARA, A. NAGY, K. P. ROOS, AND M. L. IRUELA-ARISPE, *Autocrine VEGF signaling is required for vascular homeostasis*, Cell, 130 (2007), pp. 691–703.
- [36] O. LEFEBVRE, L. SOROKIN, M. KEDINGER, AND P. SIMON-ASSMANN, *Developmental Expression and Cellular Origin of the Laminin 2, 4, and 5 Chains in the Intestine*, Developmental Biology, 210 (1999), pp. 135–150.
- [37] D. MANOUSSAKI, *A mechanochemical model of angiogenesis and vasculogenesis*, ESAIM: Mathematical Modelling and Numerical Analysis, 37 (2003), pp. 581–599.
- [38] R. M. H. MERKS, E. D. PERRY, A. SHIRINIFARD, AND J. A. GLAZIER, *Contact-inhibited chemotaxis in de novo and sprouting blood-vessel growth*, PLoS Computational Biology, 4 (2008).
- [39] T. MIURA AND R. TANAKA, *In vitro vasculogenesis models revisited-measurement of vegf diffusion in matrigel*, Mathematical Modelling of Natural Phenomena, 4 (2009), pp. 118–130.
- [40] J. MURRAY, *A mechanical theory of vascular network formation*, in Mathematical Biology, Springer, 1993, pp. 416–440.

- [41] J. D. MURRAY, *On the mechanochemical theory of biological pattern formation with application to vasculogenesis*, Comptes Rendus Biologies, 326 (2003), pp. 239–252.
- [42] P. NAMY, J. OHAYON, AND P. TRACQUI, *Critical conditions for pattern formation and in vitro tubulogenesis driven by cellular traction fields*, Journal of Theoretical Biology, 227 (2004), pp. 103–120.
- [43] K. J. PAINTER, *Mathematical models for chemotaxis and their applications in self-organisation phenomena*, Journal of Theoretical Biology, 481 (2019), pp. 162–182.
- [44] K. J. PAINTER AND T. HILLEN, *Volume-filling and quorum-sensing in models for chemosensitive movement*, Canadian Applied Mathematics Quarterly, 10 (2002), pp. 501–543.
- [45] R. PALMER, S. PRATONTEP, AND H.-G. BOYEN, *Nanostructured surfaces from size-selected clusters*, Nature Materials, 2 (2003), pp. 443–448.
- [46] T. J. POOLE, E. B. FINKELSTEIN, AND C. M. COX, *The role of FGF and VEGF in angioblast induction and migration during vascular development*, Developmental Dynamics, 220 (2001), pp. 1–17.
- [47] K. PROULX, A. LU, AND S. SUMANAS, *Cranial vasculature in zebrafish forms by angioblast cluster-derived angiogenesis*, Developmental Biology, 348 (2010), pp. 34–46.
- [48] W. RISAU AND I. FLAMME, *Vasculogenesis*, Annual Review of Cell and Developmental Biology, 11 (1995), pp. 73–91.
- [49] D. B. RUBIN, E. A. DRAB, AND K. D. BAUER, *Endothelial cell subpopulations in vitro: Cell volume, cell cycle, and radiosensitivity*, Journal of Applied Physiology, 67 (1989), pp. 1585–1590.
- [50] S. M. RUGGIERO, M. R. PILVANKAR, AND A. N. FORD VERSYPT, *Mathematical Modeling of Tuberculosis Granuloma Activation*, Processes, 5 (2017), p. 79.
- [51] F. R. SABIN, *Origin and development of the primitive vessels of the chick and of the pig*, Contributions to Embryology, 6 (1917), pp. 61–124.
- [52] S. SAFFARIAN, I. E. COLLIER, B. L. MARMER, E. L. ELSON, AND G. GOLDBERG, *Interstitial collagenase is a Brownian ratchet driven by proteolysis of collagen*, Science, 306 (2004), pp. 108–111.
- [53] M. SCIANNA, C. G. BELL, AND L. PREZIOSI, *A review of mathematical models for the formation of vascular networks*, Journal of Theoretical Biology, 333 (2013), pp. 174–209.
- [54] M. SCIANNA, L. MUNARON, AND L. PREZIOSI, *A multiscale hybrid approach for vasculogenesis and related potential blocking therapies*, Progress in Biophysics and Molecular Biology, 106 (2011), pp. 450–462.
- [55] S. SEN, A. J. ENGLER, AND D. E. DISCHER, *Matrix strains induced by cells: computing how far cells can feel*, Cellular and Molecular Bioengineering, 2 (2009), pp. 39–48.
- [56] G. SERINI, D. AMBROSI, E. GIRAUDO, A. GAMBA, L. PREZIOSI, AND F. BUSSOLINO, *Modeling the early stages of vascular network assembly*, The EMBO Journal, 22 (2003), pp. 1771–1779.
- [57] M. R. SERVEDIO, Y. BRANDVAIN, S. DHOLE, C. L. FITZPATRICK, E. E. GOLDBERG, C. A. STERN, J. VAN CLEVE, AND D. J. YEH, *Not just a theory—the utility of mathematical models in evolutionary biology*, PLoS Biology, 12 (2014).
- [58] Q. SHI, S. RAFII, M. H.-D. WU, E. S. WIJELATH, C. YU, A. ISHIDA, Y. FUJITA, S. KOTHARI, R. MOHLE, L. R. SAUVAGE, AND OTHERS, *Evidence for circulating bone marrow-derived endothelial cells*, Blood, The Journal of the American Society of Hematology, 92 (1998), pp. 362–367.

- [59] T. SHIOMI AND Y. OKADA, *MT1-MMP and MMP-7 in invasion and metastasis of human cancers*, *Cancer and Metastasis Reviews*, 22 (2003), pp. 145–152.
- [60] J. SINGH, F. HUSSAIN, AND P. DECUZZI, *Role of differential adhesion in cell cluster evolution: from vasculogenesis to cancer metastasis*, *Computer Methods in Biomechanics and Biomedical Engineering*, 18 (2015), pp. 282–292.
- [61] C. STREULI, *Extracellular matrix remodelling and cellular differentiation*, *Current Opinion in Cell Biology*, 11 (1999), pp. 634–640.
- [62] A. SZABO, E. MEHES, E. KOSA, AND A. CZIROK, *Multicellular sprouting in vitro*, *Biophysical Journal*, 95 (2008), pp. 2702–2710.
- [63] O. M. TEPPER, J. M. CAPLA, R. D. GALIANO, D. J. CERADINI, M. J. CALLAGHAN, M. E. KLEINMAN, AND G. C. GURTNER, *Adult vasculogenesis occurs through in situ recruitment, proliferation, and tubulization of circulating bone marrow-derived cells*, *Blood*, 105 (2005), pp. 1068–1077.
- [64] V. P. TERRANOVA, R. DI FLORIO, R. M. LYALL, S. HIC, R. FRIESEL, AND T. MACIAG, *Human endothelial cells are chemotactic to endothelial cell growth factor and heparin*, *Journal of Cell Biology*, 101 (1985), pp. 2330–2334.
- [65] A. TOSIN, D. AMBROSI, AND L. PREZIOSI, *Mechanics and chemotaxis in the morphogenesis of vascular networks*, *Bulletin of Mathematical Biology*, 68 (2006), pp. 1819–1836.
- [66] S. TURNER AND J. A. SHERRATT, *Intercellular adhesion and cancer invasion: a discrete simulation using the extended potts model*, *Journal of Theoretical Biology*, 216 (2002), pp. 85–100.
- [67] S. TURNER, J. A. SHERRATT, K. J. PAINTER, AND N. J. SAVILL, *From a discrete to a continuous model of biological cell movement*, *Physical Review E*, 69 (2004), p. 021910.
- [68] P. VAJKOCZY, S. BLUM, M. LAMPARTER, R. MAILHAMMER, R. ERBER, B. ENGELHARDT, D. VESTWEBER, AND A. K. HATZOPOULOS, *Multistep nature of microvascular recruitment of ex vivo-expanded embryonic endothelial progenitor cells during tumor angiogenesis*, *Journal of Experimental Medicine*, 197 (2003), pp. 1755–1765.
- [69] R. WEINER, B. A. SCHMITT, AND H. PODHAISKY, *Rowmap—a row-code with krylov techniques for large stiff odes*, *Applied Numerical Mathematics*, 25 (1997), pp. 303–319.
- [70] P. YEN, S. D. FINLEY, M. O. ENGEL-STEFANINI, AND A. S. POPEL, *A two-compartment model of VEGF distribution in the mouse*, *PloS One*, 6 (2011), p. e27514.

A mathematical model of endothelial progenitor cell cluster formation during the early stages of vasculogenesis

Supplementary Information

Chiara Villa* Alf Gerisch Mark A. J. Chaplain

In this document (supplementary information) we report supplementary material to the contents of the above named publication (main publication). In particular we include detailed linear stability analysis calculations in Section S1 and supplementary figures in Section S2 of this document.

S1 Linear stability analysis

We here conduct a linear stability analysis (LSA) on the model equations. To understand the role played by matrix degradation on the evolution of the solution of our model – and therefore its role in the early stages of cluster based vasculogenesis – particular emphasis will be put on the differences between the case in which $\gamma > 0$ and $\gamma = 0$. First we look at the full nondimensional system (13) with saturation effects, that is the one making use of definitions (2) and (14) for chemotaxis and adhesion velocity respectively. We will also consider the simplified version of the model under definitions (15) and (16) instead, corresponding to the absence of saturation effects, for a better understanding of the results of the LSA. The analysis is carried out for the 1D problem for simplicity, but in section S1.5 we will briefly consider the corresponding 2D problem.

S1.1 Spatially homogeneous steady states

The spatially homogeneous steady states of the system (13) $\bar{\mathbf{v}} = (\bar{n}, \bar{\rho}, \bar{m}, \bar{c})^\top$ satisfy

$$\begin{cases} p\bar{n}(1 - \bar{n} - \bar{\rho})_+ = 0 \\ \mu(1 - \bar{n} - \bar{\rho})_+ - \gamma\bar{\rho}\bar{m} = 0 \\ \alpha_m\bar{n} - \lambda_m\bar{m} = 0 \\ \alpha_c\bar{n} - \lambda_c\bar{c} = 0 \end{cases}, \quad (\text{S1})$$

giving either $\bar{\mathbf{v}} = (0, 1, 0, 0)^\top$ or $\bar{\mathbf{v}} = (1, 0, \alpha_m/\lambda_m, \alpha_c/\lambda_c)^\top$. Each spatially homogeneous steady state is therefore in the form

$$\bar{\mathbf{v}} = \left(\bar{n}, 1 - \bar{n}, \frac{\alpha_m}{\lambda_m}\bar{n}, \frac{\alpha_c}{\lambda_c}\bar{n} \right)^\top \quad (\text{S2})$$

*Corresponding author affiliation and email: Chiara Villa, School of Mathematics and Statistics, University of St Andrews, St Andrews KY16 9SS (UK), cv23@st-andrews.ac.uk

with either $\bar{n} = 0$ or $\bar{n} = 1$. The first one corresponds to the absence of cells, with the whole volume occupied by the ECM. On the other hand, the second one corresponds to the case in which the cells have completely degraded the ECM and are occupying the whole volume. Note that in absence of matrix degradation, *i.e.* for $\gamma = 0$, the spatially homogeneous steady states are still in the form (S2), this time with $0 \leq \bar{n} \leq 1$. We therefore have, in addition to the two states already described, infinitely many steady states in which both cells and ECM are present, filling up the volume. These additional steady states might be referred throughout this section as “intermediate” steady states, as they correspond to intermediate values of \bar{n} , namely $0 < \bar{n} < 1$.

Remark: We are going to assume that $n + \rho \leq 1$ throughout the rest of the section. That is indeed satisfied by the steady states and we justify it through the biological argument that random perturbations to these states are likely to arise naturally if there is space available, while changes that would imply $n + \rho > 1$ are much less likely as they would require high energy expenses to oppose a high pressure environment. Mathematically this allows us to avoid complications that arise when introducing perturbations in the typical ansatz (*vid.* below) due to definitions (2), (7) and (8). In fact, under this assumption the term $(1 - n - \rho)_+ = (1 - n - \rho) \geq 0$ for all perturbations allowed.

S1.2 Stability under spatially homogeneous perturbations

Introducing a small spatially homogeneous perturbation $\mathbf{v} = \bar{\mathbf{v}} + \tilde{\mathbf{v}}(t)$, with $|\tilde{\mathbf{v}}| \ll 1$, in (13) and linearising leads to the following system for the perturbation $\tilde{\mathbf{v}}(t)$:

$$\begin{cases} \partial_t \tilde{n} = -p\bar{n}(\tilde{n} + \tilde{\rho}) \\ \partial_t \tilde{\rho} = -\gamma(\bar{\rho}\tilde{n} + \bar{m}\tilde{\rho}) - \mu(\tilde{n} + \tilde{\rho}) \\ \partial_t \tilde{m} = \alpha_m \tilde{n} - \lambda_m \tilde{m} \\ \partial_t \tilde{c} = \alpha_c \tilde{n} - \lambda_c \tilde{c} \end{cases} \quad (\text{S3})$$

Assuming small perturbations in the form $\tilde{n}, \tilde{\rho}, \tilde{m}, \tilde{c} \propto \exp(\sigma t)$, the system (S3) can be rewritten as

$$\mathbf{M}\tilde{\mathbf{v}} = \mathbf{0}, \quad \text{with} \quad \mathbf{M} = \begin{pmatrix} \sigma + p\bar{n} & p\bar{n} & 0 & 0 \\ \mu & \sigma + \gamma\bar{m} + \mu & \gamma\bar{\rho} & 0 \\ -\alpha_m & 0 & \sigma + \lambda_m & 0 \\ -\alpha_c & 0 & 0 & \sigma + \lambda_c \end{pmatrix}. \quad (\text{S4})$$

For a non-trivial solution we require $\det \mathbf{M} = 0$, leading to the dispersion relation

$$(\sigma + \lambda_m)(\sigma + \lambda_c) \left[\sigma^2 + \sigma(p\bar{n} + \gamma\bar{m} + \mu) + \gamma p\bar{n}\bar{m} \right] + \alpha_m \gamma p\bar{n}\bar{\rho}(\sigma + \lambda_c) = 0, \quad (\text{S5})$$

which can only be satisfied for $\text{Re}(\sigma) < 0$, indicating both spatially homogeneous steady states are stable under spatially homogeneous perturbations. The same conclusion can be quickly reached for all the additional spatially homogeneous steady states in absence of matrix degradation, *i.e.* for $\gamma = 0$ as we obtain the corresponding version of the dispersion relation (S5).

S1.3 Stability under spatially inhomogeneous perturbations

Let us now introduce spatially inhomogeneous perturbations $\mathbf{v} = \bar{\mathbf{v}} + \tilde{\mathbf{v}}(t, x)$, with $|\tilde{\mathbf{v}}| \ll 1$. Given that $\bar{n} + \bar{\rho} = 1$ and $\gamma\bar{\rho}\bar{n} = \gamma\bar{\rho}\bar{m} = \gamma\bar{\rho}\bar{c} = 0$ for all spatially homogeneous steady states, after linearisation

system (13) gives

$$\begin{cases} \partial_t \tilde{n} = D_n \Delta \tilde{n} - \bar{n} \nabla \cdot \mathcal{A}[\bar{\mathbf{v}} + \tilde{\mathbf{v}}(t, \cdot)] - p\bar{n}(\tilde{n} + \tilde{\rho}) \\ \partial_t \tilde{\rho} = -\gamma(\bar{\rho}\tilde{m} + \bar{m}\tilde{\rho}) - \mu(\tilde{n} + \tilde{\rho}) \\ \partial_t \tilde{m} = D_m \Delta \tilde{m} + \alpha_m \tilde{n} - \lambda_m \tilde{m} \\ \partial_t \tilde{c} = D_c \Delta \tilde{c} + \alpha_c \tilde{n} - \lambda_c \tilde{c} \end{cases}. \quad (\text{S6})$$

We immediately notice that, as all steady states satisfy volume filling conditions, chemotaxis in presence of saturating effects does not play a role in the dynamics of small perturbations from any of these states.

Then, after linearisation, for the 1D problem $\mathcal{A}[\bar{\mathbf{v}} + \tilde{\mathbf{v}}(t, \cdot)]$ in equation (S6)₁ becomes

$$\mathcal{A}[\bar{\mathbf{v}} + \tilde{\mathbf{v}}(t, \cdot)](x) = -\frac{1}{R}(S_{nn}\bar{n} + S_{n\rho}\bar{\rho}) \int_0^R \sum_{j=0}^1 \eta(j) \Gamma(r) (\tilde{n}(t, x + r\eta(j)) + \tilde{\rho}(t, x + r\eta(j))) dr \quad (\text{S7})$$

with $\Gamma(r)$ given by the corresponding definition in (6).

Assuming small perturbations in the form $\tilde{n}, \tilde{\rho}, \tilde{m}, \tilde{c} \propto \exp(\sigma t + ikx)$, note first of all that (S7) can be rewritten as

$$\begin{aligned} \mathcal{A}[\bar{\mathbf{v}} + \tilde{\mathbf{v}}(t, \cdot)](x) &= -\frac{1}{R}(S_{nn}\bar{n} + S_{n\rho}\bar{\rho}) (\tilde{n}(x) + \tilde{\rho}(x)) \int_0^R \Gamma(r) (\exp(ikr) - \exp(-ikr)) \\ &= -\frac{1}{R}(S_{nn}\bar{n} + S_{n\rho}\bar{\rho}) (\tilde{n}(x) + \tilde{\rho}(x)) \frac{2i}{R} \int_0^R \left(1 - \frac{r}{R}\right) \sin(kr) dr \\ &= -\frac{2i}{R^2 k} (S_{nn}\bar{n} + S_{n\rho}\bar{\rho}) (\tilde{n}(x) + \tilde{\rho}(x)) \left(1 - \frac{1}{Rk} \sin(Rk)\right). \end{aligned} \quad (\text{S8})$$

We will make use of the notation

$$w_1(k) := \left(1 - \frac{1}{Rk} \sin(Rk)\right), \quad (\text{S9})$$

for which we have that $w_1(k) \geq 0$ for all $k \in \mathbb{R}$. Then, for small perturbations in the form introduced above, the system (S6) can be rewritten as

$$\mathbf{M}\tilde{\mathbf{v}} = \mathbf{0}, \text{ with } \mathbf{M} = \begin{pmatrix} \sigma + D_n k^2 + A(k) + p\bar{n} & A(k) + p\bar{n} & 0 & 0 \\ \mu & \sigma + \gamma\bar{m} + \mu & \gamma\bar{\rho} & 0 \\ -\alpha_m & 0 & \sigma + D_m k^2 + \lambda_m & 0 \\ -\alpha_c & 0 & 0 & \sigma + D_c k^2 + \lambda_c \end{pmatrix}, \quad (\text{S10})$$

where

$$A(k) = \frac{2\bar{n}}{R^2} (S_{nn}\bar{n} + S_{n\rho}\bar{\rho}) w_1(k), \quad (\text{S11})$$

with $w_1(k)$ defined in (S9). This immediately implies $A(k) \geq 0$ for all steady states, those with and without matrix degradation, and in particular $A(k) = 0$ for $\bar{n} = 0$. The dispersion relation $\sigma(k^2)$ can then be obtained by imposing $\det \mathbf{M} = 0$ for a non-trivial solution to (S10), and in order for the steady states to be unstable to spatially inhomogeneous perturbations – and patterns to arise – we require $\text{Re}(\sigma(k^2)) > 0$ for some $k^2 \in \mathbb{R}$. This, in its more general form, is given by

$$(\sigma + D_c k^2 + \lambda_c)(p\bar{n} + A(k))[\sigma + \gamma\bar{m} + (\sigma + D_n k^2)(\sigma + \gamma\bar{m} + \mu)] = 0, \quad (\text{S12})$$

where we have used the fact that $\gamma\bar{n}\bar{\rho} = 0$ for all steady states considered. It is clear from (S12) that $\text{Re}(\sigma(k^2)) < 0$ for all k^2 . Therefore all steady states considered are also stable to spatially inhomogeneous perturbations. We claim this to be due to saturation effects introduced in (2) and (7), while we may still expect chemotaxis and cell-to-cell or cell-to-matrix adhesion to play an important role for cell aggregation when the initially perturbed states are far from being volume filling. Let us explore the matter further in the next section.

S1.4 Considerations in absence of saturation effects

We here consider the pattern formation potential of the model in absence of saturation effects, that is we make use of definition (15) for chemotaxis and of (16) for the adhesion velocity $g(\mathbf{v})$. All results and considerations made in sections S1.1 and S1.2 on spatially homogeneous steady states and their stability under spatially homogeneous perturbations still hold. Introducing spatially inhomogeneous perturbations as in section S1.3 leads to the following linearised system alternative to (S6):

$$\begin{cases} \partial_t \tilde{n} = D_n \Delta \tilde{n} - \chi \bar{n} \Delta \tilde{c} - \bar{n} \nabla \cdot \mathcal{A}[\bar{\mathbf{v}} + \tilde{\mathbf{v}}(t, \cdot)] - p\bar{n}(\tilde{n} + \tilde{\rho}) \\ \partial_t \tilde{\rho} = -\gamma(\bar{\rho}\tilde{m} + \bar{m}\tilde{\rho}) - \mu(\tilde{n} + \tilde{\rho}) \\ \partial_t \tilde{m} = D_m \Delta \tilde{m} + \alpha_m \tilde{n} - \lambda_m \tilde{m} \\ \partial_t \tilde{c} = D_c \Delta \tilde{c} + \alpha_c \tilde{n} - \lambda_c \tilde{c} \end{cases}, \quad (\text{S13})$$

in which, for the 1D problem, $\mathcal{A}[\bar{\mathbf{v}} + \tilde{\mathbf{v}}(t, \cdot)]$ is given by

$$\mathcal{A}[\bar{\mathbf{v}} + \tilde{\mathbf{v}}(t, \cdot)](x) = \frac{1}{R} \int_0^R \sum_{j=0}^1 \eta(j) \Gamma(r) (S_{nn} \tilde{n}(t, x + r\eta(j)) + S_{n\rho} \tilde{\rho}(t, x + r\eta(j))) dr \quad (\text{S14})$$

with $\Gamma(r)$ given by the corresponding definition in (6). Notice that under these modelling assumptions – namely no saturation effects included in the adhesion velocity – we do not need to assume $n + \rho \leq 1$ for analytical tractability, and therefore have no crafty restrictions on the perturbations introduced. Then, assuming small perturbations in the form $\tilde{n}, \tilde{\rho}, \tilde{m}, \tilde{c} \propto \exp(\sigma t + ikx)$, (S14) can be rewritten as

$$\begin{aligned} \mathcal{A}[\bar{\mathbf{v}} + \tilde{\mathbf{v}}(t, \cdot)](x) &= \frac{1}{R} (S_{nn} \tilde{n}(x) + S_{n\rho} \tilde{\rho}(x)) \int_0^R \Gamma(r) (\exp(ikr) - \exp(-ikr)) \\ &= \frac{1}{R} (S_{nn} \tilde{n}(x) + S_{n\rho} \tilde{\rho}(x)) \frac{2i}{R} \int_0^R \left(1 - \frac{r}{R}\right) \sin(kr) dr \\ &= \frac{2i}{R^2 k} (S_{nn} \tilde{n}(x) + S_{n\rho} \tilde{\rho}(x)) w_1(k), \end{aligned} \quad (\text{S15})$$

with $w_1(k) \geq 0$ defined in (S9). We can then rewrite (S13) as $\mathbf{M}\tilde{\mathbf{v}} = \mathbf{0}$, with \mathbf{M} given by

$$\mathbf{M} = \begin{pmatrix} \sigma + D_n k^2 - A_n(k) + p\bar{n} & -A_\rho(k) + p\bar{n} & 0 & -\chi\bar{n}k^2 \\ \mu & \sigma + \gamma\bar{m} + \mu & \gamma\bar{\rho} & 0 \\ -\alpha_m & 0 & \sigma + D_m k^2 + \lambda_m & 0 \\ -\alpha_c & 0 & 0 & \sigma + D_c k^2 + \lambda_c \end{pmatrix}, \quad (\text{S16})$$

where

$$A_n(k) = \frac{2\bar{n}}{R^2} S_{nn} w_1(k) \quad \text{and} \quad A_\rho(k) = \frac{2\bar{n}}{R^2} S_{n\rho} w_1(k). \quad (\text{S17})$$

We have both $A_n(k) \geq 0$ and $A_\rho(k) \geq 0$ for all $k \in \mathbb{R}$, and $A_n(k) = A_\rho(k) = 0$ for $\bar{n} = 0$. Comparing these to (S10) and (S11), we see that in absence of saturation effects the contributions from cell-to-cell and cell-to-matrix adhesion are decoupled and both give a negative contribution to \mathbf{M} . Furthermore, the contribution from chemotaxis only vanishes for $\bar{n} = 0$. From this system the dispersion relation $\sigma(k^2)$ satisfies

$$\begin{aligned} (\sigma + D_m k^2 + \lambda_m) \left\{ \left[(\sigma + D_n k^2) (\sigma + \gamma\bar{m} + \mu) + (p\bar{n} - A_n(k)) (\sigma + \gamma\bar{m}) \right. \right. \\ \left. \left. + \mu (A_\rho(k) - A_n(k)) \right] (\sigma + D_c k^2 + \lambda_c) - \alpha_c \chi \bar{n} k^2 (\sigma + \gamma\bar{m} + \mu) \right\} = 0. \end{aligned} \quad (\text{S18})$$

We have again that the steady state corresponding to $\bar{n} = 0$ is stable to spatially inhomogeneous perturbations. On the contrary, the steady state corresponding to $\bar{n} = 1$, as well as the intermediate ones in absence of matrix degradation, may be unstable to spatially inhomogeneous perturbations for strong enough cell-to-cell adhesion and/or chemotaxis, *i.e.* for large enough S_{nn} and α_c and/or χ . In addition, the magnitude of cell-to-cell adhesion $A_n(k)$ in (S17) will be larger for smaller values of the sensing radius R and larger values of \bar{n} , and the contribution from chemotactic movement will also increase for larger values of \bar{n} . Therefore in absence of saturation effects steady states corresponding to $\bar{n} > 0$ may be unstable to spatially inhomogeneous perturbations and patterns may form. This suggests that perturbed initial conditions far from being volume filling, so that saturation effects do not play a big role, might result in cell aggregation thanks to cell-to-cell adhesion and chemotaxis, as long as the initial cell density is large enough for these dynamics to play a significant role.

S1.5 Extension of LSA results to the 2D problem

We here consider how the results obtained so far change in the 2D problem. Conclusions drawn in sections S1.1 and S1.2 remain unchanged.

Considerations in presence of saturation effects. When introducing spatially inhomogeneous perturbations $\mathbf{v} = \bar{\mathbf{v}} + \tilde{\mathbf{v}}(t, \mathbf{x})$, after linearisation $\mathcal{A}[\bar{\mathbf{v}} + \tilde{\mathbf{v}}(t, \cdot)](\mathbf{x})$ for the 2D problem is given by

$$\mathcal{A}[\bar{\mathbf{v}} + \tilde{\mathbf{v}}(t, \cdot)](\mathbf{x}) = -\frac{1}{R} (S_{nn}\bar{n} + S_{n\rho}\bar{\rho}) \int_0^R r \int_0^{2\pi} \boldsymbol{\eta}(\theta) \Gamma(r) (\tilde{n}(t, \mathbf{x} + r\boldsymbol{\eta}(\theta)) + \tilde{\rho}(t, \mathbf{x} + r\boldsymbol{\eta}(\theta))) d\theta dr \quad (\text{S19})$$

with $\Gamma(r)$ given by the corresponding definition in (6). Assuming small perturbations in the form $\tilde{n}, \tilde{\rho}, \tilde{m}, \tilde{c} \propto \exp(\sigma t + i\mathbf{k} \cdot \mathbf{x})$, with $\mathbf{k} = (k_1, k_2)^\top \in \mathbb{R}^2$, then (S19) can be rewritten as

$$\begin{aligned}
\mathcal{A}[\tilde{\mathbf{v}} + \tilde{\mathbf{v}}(t, \cdot)](\mathbf{x}) &= -\frac{1}{R}(S_{nn}\bar{n} + S_{n\rho}\bar{\rho})(\tilde{n}(\mathbf{x}) + \tilde{\rho}(\mathbf{x})) \int_0^R r \int_0^{2\pi} \boldsymbol{\eta}(\theta) \Gamma(r) \exp(ir\mathbf{k} \cdot \boldsymbol{\eta}(\theta)) d\theta dr \\
&= -\frac{1}{R}(S_{nn}\bar{n} + S_{n\rho}\bar{\rho})(\tilde{n}(\mathbf{x}) + \tilde{\rho}(\mathbf{x})) \int_0^{2\pi} \boldsymbol{\eta}(\theta) \int_0^R r \Gamma(r) \exp(ir\mathbf{k} \cdot \boldsymbol{\eta}(\theta)) dr d\theta \\
&= -\frac{1}{R}(S_{nn}\bar{n} + S_{n\rho}\bar{\rho})(\tilde{n}(\mathbf{x}) + \tilde{\rho}(\mathbf{x})) \frac{3}{\pi R^2} \int_0^{2\pi} \boldsymbol{\eta}(\theta) \int_0^R r \left(1 - \frac{r}{R}\right) \exp(ir\mathbf{k} \cdot \boldsymbol{\eta}(\theta)) dr d\theta \\
&= \frac{3}{\pi R^3}(S_{nn}\bar{n} + S_{n\rho}\bar{\rho})(\tilde{n}(\mathbf{x}) + \tilde{\rho}(\mathbf{x})) \left[\Theta_I(\mathbf{k}) + i\Theta_R(\mathbf{k})\right]
\end{aligned} \tag{S20}$$

where we have defined, with notation that will become more intuitive in a few steps,

$$\Theta_R(\mathbf{k}) = \int_0^{2\pi} \frac{\boldsymbol{\eta}(\theta)}{(\mathbf{k} \cdot \boldsymbol{\eta}(\theta))^2} \left[\sin(R\mathbf{k} \cdot \boldsymbol{\eta}(\theta)) + \frac{2}{R\mathbf{k} \cdot \boldsymbol{\eta}(\theta)} \left(\cos(R\mathbf{k} \cdot \boldsymbol{\eta}(\theta)) - 1 \right) \right] d\theta, \tag{S21}$$

$$\Theta_I(\mathbf{k}) = \int_0^{2\pi} \frac{\boldsymbol{\eta}(\theta)}{(\mathbf{k} \cdot \boldsymbol{\eta}(\theta))^2} \left[1 + \cos(R\mathbf{k} \cdot \boldsymbol{\eta}(\theta)) + \frac{2}{R\mathbf{k} \cdot \boldsymbol{\eta}(\theta)} \sin(R\mathbf{k} \cdot \boldsymbol{\eta}(\theta)) \right] d\theta. \tag{S22}$$

We eventually obtain the system (S10), in which $k^2 = |\mathbf{k}|^2 = k_1^2 + k_2^2$ and, instead of $A(k)$ as in (S11), we have $A(\mathbf{k})$ given by

$$A(\mathbf{k}) = -\frac{3\bar{n}}{\pi R^3}(S_{nn}\bar{n} + S_{n\rho}\bar{\rho}) \mathbf{k} \cdot \left[\Theta_R(\mathbf{k}) - i\Theta_I(\mathbf{k}) \right], \tag{S23}$$

with $\Theta_R(\mathbf{k})$ and $\Theta_I(\mathbf{k})$ defined in (S21). While these integrals are fairly complex, they can be evaluated numerically (we have used the trapezoidal rule for numerical integration). This allowed us to conclude that, just like in the 1D case, $\text{Re}(A(\mathbf{k})) \geq 0$ for all $\mathbf{k} \in \mathbb{R}^2$. For this problem we therefore obtain the corresponding version of equation (S12) for the dispersion relation and reach the same conclusions as in section S1.3 for the full system including saturation effects.

Considerations in absence of saturation effects. In absence of saturation effects, $\mathcal{A}[\tilde{\mathbf{v}} + \tilde{\mathbf{v}}(t, \cdot)](\mathbf{x})$ is given by the 2D correspondent of equation (S14), that is

$$\mathcal{A}[\tilde{\mathbf{v}} + \tilde{\mathbf{v}}(t, \cdot)](\mathbf{x}) = \frac{1}{R} \int_0^R r \int_0^{2\pi} \boldsymbol{\eta}(\theta) \Gamma(r) \left(S_{nn} \tilde{n}(t, \mathbf{x} + r\boldsymbol{\eta}(\theta)) + S_{n\rho} \tilde{\rho}(t, \mathbf{x} + r\boldsymbol{\eta}(\theta)) \right) d\theta dr. \tag{S24}$$

Then assuming small perturbations in the form $\tilde{n}, \tilde{\rho}, \tilde{m}, \tilde{c} \propto \exp(\sigma t + i\mathbf{k} \cdot \mathbf{x})$, with $\mathbf{k} = (k_1, k_2)^\top \in \mathbb{R}^2$,

(S24) can be rewritten as

$$\begin{aligned}
\mathcal{A}[\bar{\mathbf{v}} + \tilde{\mathbf{v}}(t, \cdot)](\mathbf{x}) &= \frac{1}{R} (S_{nn} \tilde{n}(\mathbf{x}) + S_{n\rho} \tilde{\rho}(\mathbf{x})) \int_0^R r \int_0^{2\pi} \boldsymbol{\eta}(\theta) \Gamma(r) \exp(ir\mathbf{k} \cdot \boldsymbol{\eta}(\theta)) d\theta dr \\
&= \frac{1}{R} ((S_{nn} \tilde{n}(\mathbf{x}) + S_{n\rho} \tilde{\rho}(\mathbf{x})) \int_0^{2\pi} \boldsymbol{\eta}(\theta) \int_0^R r \Gamma(r) \exp(ir\mathbf{k} \cdot \boldsymbol{\eta}(\theta)) dr d\theta \\
&= \frac{1}{R} (S_{nn} \tilde{n}(\mathbf{x}) + S_{n\rho} \tilde{\rho}(\mathbf{x})) \frac{3}{\pi R^2} \int_0^{2\pi} \boldsymbol{\eta}(\theta) \int_0^R r \left(1 - \frac{r}{R}\right) \exp(ir\mathbf{k} \cdot \boldsymbol{\eta}(\theta)) dr d\theta \\
&= -\frac{3}{\pi R^3} (S_{nn} \tilde{n}(\mathbf{x}) + S_{n\rho} \tilde{\rho}(\mathbf{x})) \left[\Theta_I(\mathbf{k}) + i \Theta_R(\mathbf{k}) \right],
\end{aligned} \tag{S25}$$

with $\Theta_R(\mathbf{k})$ and $\Theta_I(\mathbf{k})$ defined in (S21). We eventually end up with a system $\mathbf{M}\tilde{\mathbf{v}} = \mathbf{0}$, with \mathbf{M} defined as in (S16), in which again we have $k^2 = |\mathbf{k}|^2 = k_1^2 + k_2^2$ and, instead of $A_n(k)$ and $A_\rho(k)$ as in (S17), $A_n(\mathbf{k})$ and $A_\rho(\mathbf{k})$ defined by

$$A_n(\mathbf{k}) = -\frac{3\bar{n}}{\pi R^3} S_{nn} \mathbf{k} \cdot \left[\Theta_R(\mathbf{k}) - i \Theta_I(\mathbf{k}) \right] \quad \text{and} \quad A_\rho(\mathbf{k}) = -\frac{3\bar{n}}{\pi R^3} S_{n\rho} \mathbf{k} \cdot \left[\Theta_R(\mathbf{k}) - i \Theta_I(\mathbf{k}) \right]. \tag{S26}$$

Again, we have verified numerically that $\text{Re}(A_n(\mathbf{k})) \geq 0$ and $\text{Re}(A_\rho(\mathbf{k})) \geq 0$ for all $\mathbf{k} \in \mathbb{R}^2$, and can therefore reach analogous conclusions to those drawn in section S1.4 for the corresponding 2D problem.

S2 Supplementary figures

Figure S1 contains plot analogous to those in Figures 6 and 7 in the main publication, with additional information complementing the results presented in Section 3.4 of the main publication. In particular the plots display how choosing parameter values of different orders of magnitude compared to those chosen for the baseline parameter set (see Table 1 in the main publication) will influence average cluster width W and compactness C , for the parameter D_c (Figure S1a), γ (Figure S1b), D_m (Figure S1c), S_{nn} (Figure S1d) and D_n (Figure S1e).

Figure S2 contains plots of the two-dimensional simulations under the baseline parameter set shown in the second row of Figures 8, 9 and 10 of the main publication, displaying the solution at additional times, showing the long-term behaviour of the solution.

Figure S3 contains plots of the two-dimensional simulations under the baseline parameter set in absence of matrix degradation (*i.e.* $\gamma = 0$), starting from the same initial conditions (*cf.* first panel in first row of Figure S2).

Figure S4 contains plots of the two-dimensional simulations under the baseline parameter set (second row) and under different values of the MMP secretion rate α_m , starting from the same initial conditions (*cf.* first panel in first row of Figure S2).

Figure S5 contains plots of the two-dimensional simulations under the baseline parameter set (second row) and under different values of the VEGF secretion rate α_c , starting from the same initial conditions (*cf.* first panel in first row of Figure S2).

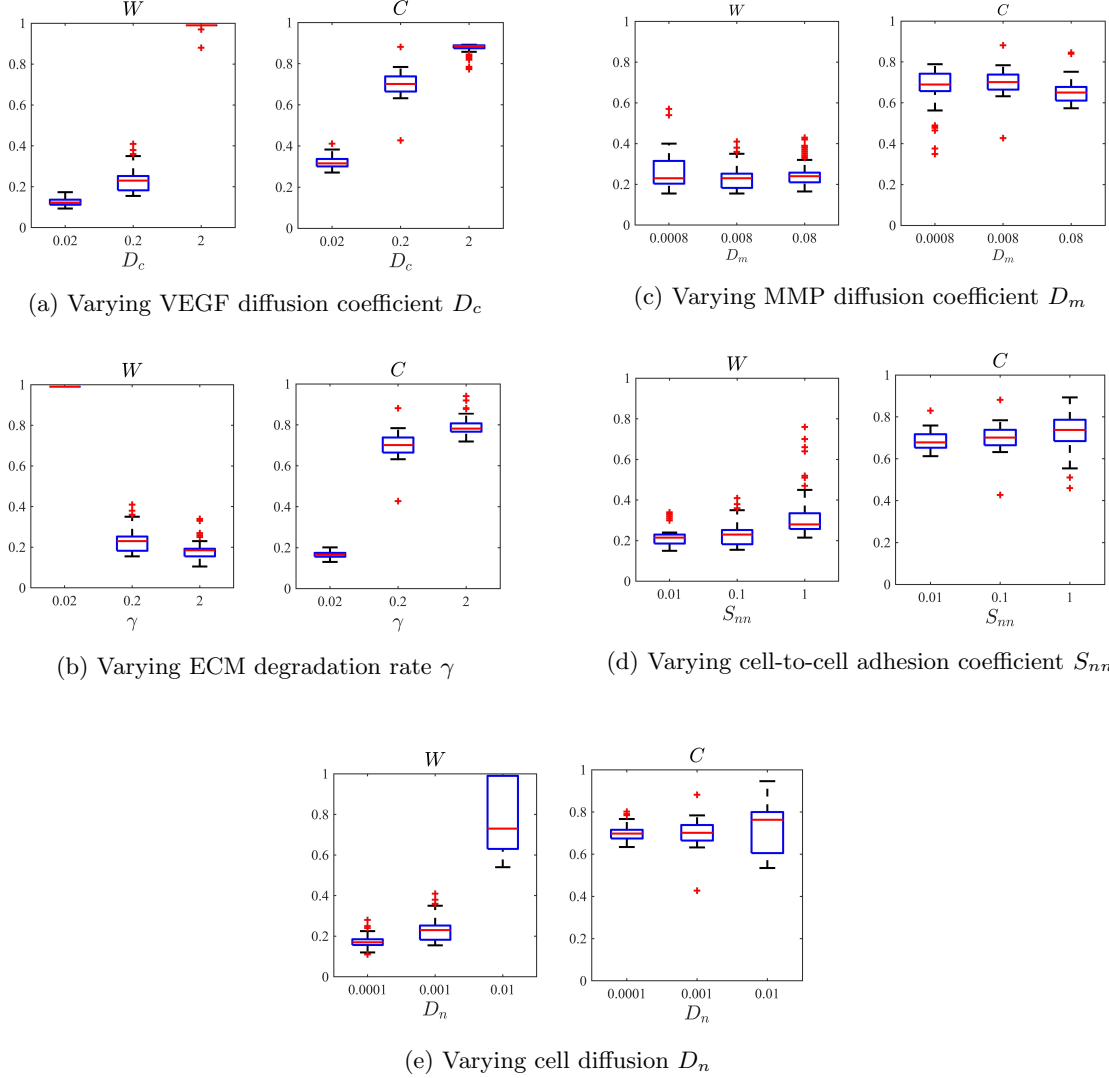


Figure S1: Cluster width W and compactness C , defined in (19) and (20), under variations of certain parameters from the baseline parameter set (BPS), in Table 1 of the main publication. In (a) we have boxplots of W and C measured on the numerical solution of the system (13) at $t = 50$, for D_c taking its value in the BPS (center), one order of magnitude higher (left) and one order of magnitude lower (right) than the one in the BPS. Each boxplot collects data from 100 simulations under randomised initial conditions (11) and (12)₁. In (b)-(e) we have the same as in (a) but varying parameters γ (b), D_m (c), S_{nn} (d) and D_n (e).

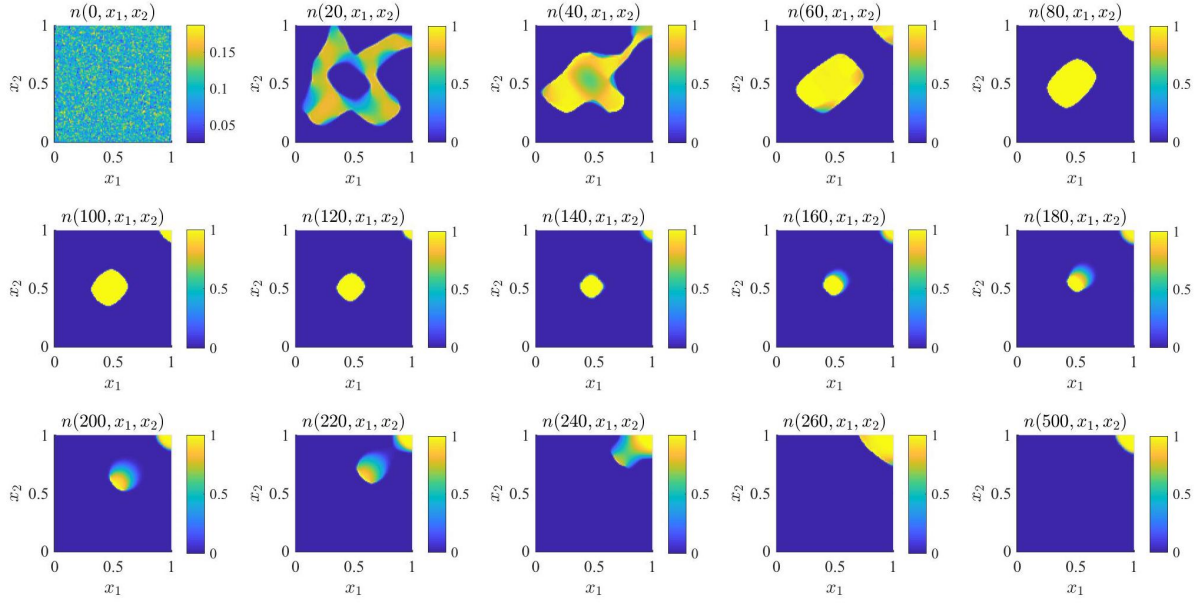


Figure S2: Plots of the cell density $n(t, x)$ obtained solving the system (13), together with definitions (5), (6) and (14), initial conditions (11) and (12)₂, complemented with zero Neumann boundary conditions, under the parameter choices reported in Table 1. The solution is plotted at time $t = 0, 20, 40, 60, 80$ (first row, left to right), $t = 100, 120, 140, 160, 180$ (second row, left to right) and $t = 200, 220, 240, 260, 500$ (third row, left to right).

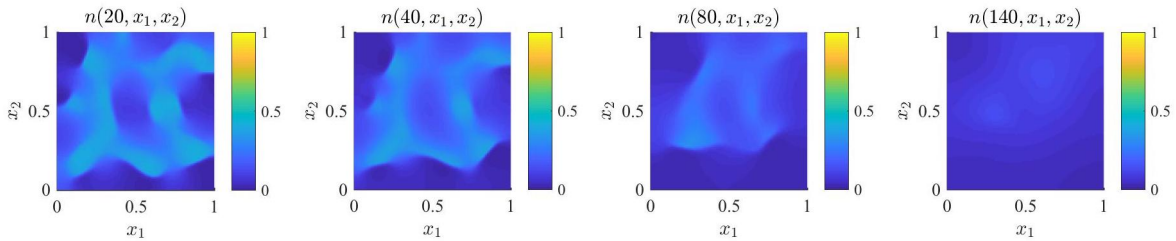


Figure S3: Plots of the cell density $n(t, x)$ obtained solving the system (13), together with definitions (5), (6) and (14), initial conditions (11) and (12)₂, complemented with zero Neumann boundary conditions, under the parameter choices reported in Table 1, except for $\gamma = 0$. The solution is plotted at time $t = 20$ (first panel), $t = 40$ (second panel), $t = 80$ (third panel) and $t = 140$ (fourth panel).

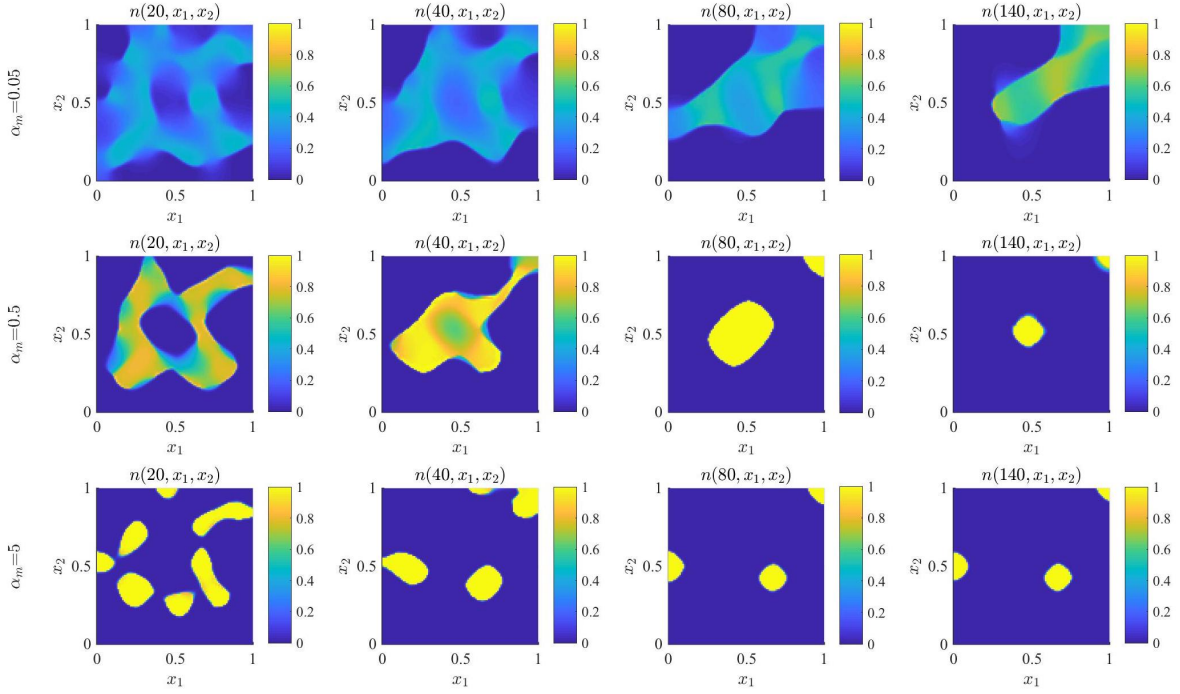


Figure S4: **First row:** Plots of the cell density $n(t, x)$ obtained solving the system (13), together with definitions (5), (6) and (14), initial conditions (11) and (12)₂, complemented with zero Neumann boundary conditions, under the parameter choices reported in Table 1, except for $\alpha_m = 0.05$. The solution is plotted at time $t = 20$ (first panel), $t = 40$ (second panel), $t = 80$ (third panel) and $t = 140$ (fourth panel). **Second and third row:** Same as first row, except for $\alpha_m = 0.5$ (second row) and $\alpha_m = 5$ (third row).

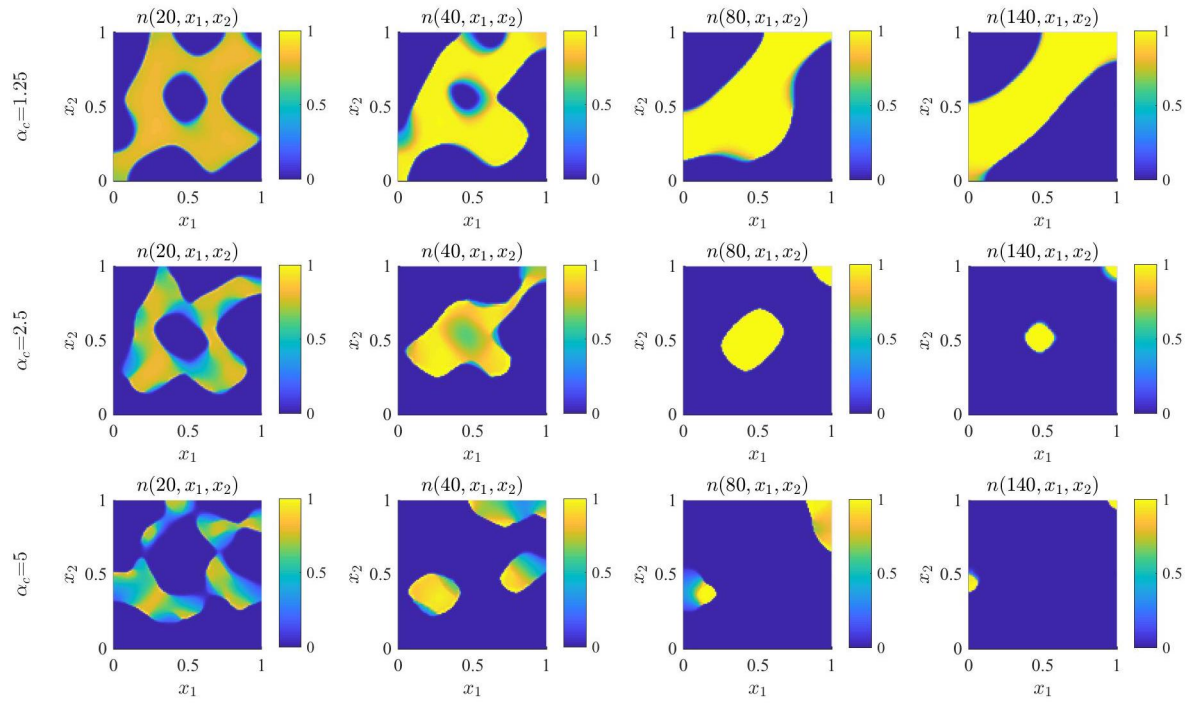


Figure S5: **First row:** Plots of the cell density $n(t, x)$ obtained solving the system (13), together with definitions (5), (6) and (14), initial conditions (11) and (12)₂, complemented with zero Neumann boundary conditions, under the parameter choices reported in Table 1, except for $\alpha_c = 1.25$. The solution is plotted at time $t = 20$ (first panel), $t = 40$ (second panel), $t = 80$ (third panel) and $t = 140$ (fourth panel). **Second and third row:** Same as first row, except for $\alpha_c = 2.5$ (second row) and $\alpha_c = 5$ (third row).